ارائه شده توسط:

سایت ترجمه فا

مرجع جدیدترین مقالات ترجمه شده

از نشریات معتبر

Available online at www.sciencedirect.com
ScienceDirect
Composites: Part B 38 (2007) 448–468
composites
Part B: engineering
www.elsevier.com/locate/compositesb

Response of fiber reinforced composites to underwater explosive loads

R.C. Batra *, N.M. Hassan [1]

Department of Engineering Science and Mechanics, MIC 0219, Virginia Polytechnic Institute and State University, Blacksburg, VA 24061, United States

Received 26 April 2006; accepted 7 September 2006
Available online 17 November 2006

Abstract

An in-house developed, verified and fully validated three-dimensional finite element code, with rate dependent damage evolution equations for anisotropic bodies, is used to numerically ascertain the damage developed in a fiber-reinforced composite due to shock loads representative of those produced by an underwater explosion. Three internal variables characterize damage due to fiber/matrix debonding, fiber breakage, and matrix cracking. The delamination and relative sliding of adjoining layers has been simulated by the nodal release technique. The interaction among the four failure modes, and the possibility of their initiating concurrently at one or more points in the composite is considered. The effect of different parameters on the damage development and propagation, and energy absorbed in each one of the four failure modes has been examined. These results give preliminary information on composite structure's design for maximizing the energy absorption and hence increasing structure's resistance to blast loads. The paper is a sequel to Hassan and Batra's paper [Composites B, 2007] wherein details of the damage model, verification of the code, and the validation of the mathematical model are given.

Keywords: A. Polymer–matrix composites (PMCs); B. Impact behavior; C. Damage mechanics; C. Energy dissipated; C. Figure of merit; C. Finite element analysis (FEA)

1. Introduction

A major threat to ship structures and marine vessels is being exposed to severe shock loads [1,2] which could be due to the underwater explosion of a mine or a torpedo, the structure striking a partially submerged object in water, and/or the slamming pressure that occurs at high sea states when the forefront of the vessel rises above the water surface and then rapidly reenters the water. These shock waves generally generate impulses of very high pressures but short durations, resulting in extremely high strain rates, which may cause severe structural damage.

In order to decrease weight of the empty ship and thus increase payload, there is significant interest in developing lightweight structures for replacing conventional plate–beam metallic components in selected areas of a ship. For such structures to provide adequate protection against underwater blast, they must have high resistance to impulsive loads and good residual (post-impact) strength [3]. The estimation of service life requires knowing the progressive degradation of material properties as a consequence of growth of the internal damage. The absorption of energy in ballistic situations depends on the evolution of damage in the target that progressively degrades its material properties. Although several models have been developed to describe the deformation mechanisms of composites, no one model adequately characterizes the entire process due to numerous factors like the difference in behavior between fiber types, fabric and composite constructions, the variation in thermomechanical properties, ductility, anisotropy, rate sensitivity of composite materials, and the fact that composite materials respond differently from monolithic materials (e.g., a metal) upon which fundamentals of the mechanics of high strain rate deformation are based [4].

The initiation and propagation of damage in composites due to impulsive loads has been studied experimentally, analytically and numerically. For underwater shock and

* Corresponding author.
E-mail address: rbatra@vt.edu (R.C. Batra).
[1] Present address: Department of Industrial Engineering, Alhosn University, Abu Dhabi, UAE.

1359-8368/$ - see front matter © 2006 Elsevier Ltd. All rights reserved.
doi:10.1016/j.compositesb.2006.09.001

air blast loading, tests are usually performed by subjecting large composite panels (up to 3 m × 3 m in size) or full scale sections of a ship to increasing levels of shock loads and then examining the laminate for evidence of gross structural damage [1] due to fiber breakage, matrix cracking, fiber/matrix debonding, and delamination.

Mouritz [3] used the four-point bend test to measure the residual flexural strength of a glass reinforced polymer (GRP) laminate after it had been impulsively loaded by an underwater shock wave produced by an explosion. The examination by a scanning electron microscope of the laminate tested at a shock pressure of 8 MPa revealed that damage was confined to some cracking of the polymer matrix and a small number of short delaminations; consequently, the flexural strength remained essentially unchanged. However, when the peak pressure of the shock wave exceeded 8 MPa, the laminate was severely damaged by cracking of the polymer, breakage and buckling of fibers, and large delamination zones. High compressive stresses in the area near the impacted surface buckled glass fibers there, and high tensile stresses near the back surface caused cracking of the polymer and glass fibers there. Throughout the laminate, extensive delamination occurred at many interfaces between adjoining plies. The extent of damage, as evidenced by the progressive deterioration of the residual flexural strength and stiffness, increased with an increase in the intensity of the shock pressure from 8 to 28 MPa. Will et al. [5] have pointed out that for high velocity impacts the structure responds in a local mode, a little energy is used to deform fibers and the structure, and a significant amount of energy is dissipated in mechanisms such as delamination, debonding and fiber pull-out. In the remainder of this Section, we summarize literature results regarding effects of different material, geometric and loading parameters on structure's response to impulsive loads.

1.1. Target thickness

Thick laminates respond differently to externally applied loads than thin laminates [6]. Morais et al. [7] studied the effect of the laminate thickness on the resistance of 12.5 cm × 12.5 cm carbon, glass and aramid fabric composites to repeated low energy drop weight impacts with the weight dropped from a height of 0.5–1.0 m at the specimen center. For impact energies below 3.7 J, the resistance to repeated low energy impacts increases with laminate thickness, irrespective of the type of fiber used to reinforce the composite. However, for high impact energies, the resistance of the laminate to repeated impacts depends not only on its thickness but also on the type of fibers and their spatial distribution [7]. Gellert et al. [4] studied experimentally the effect of the target thickness on the ballistic perforation of GRPs. For thin targets the damage was in the form of a delamination cone opening towards the exit side; its diameter and height increased with an increase in the target thickness, until for sufficiently thick targets the delamination cone opened towards the impact side. The diameter of the delaminated zone on the target impact side was found to increase linearly with the target thickness from when it first appeared there, and that on the target exit side increase with the target thickness until it plateaued. Gellert et al. [4] also observed a transition in energy absorption, which they postulated as being due to a change in perforation mechanism from largely dishing in thin targets to a combination of indentation and dishing in thick targets. The target thickness at which this transition occurs depends on the projectile diameter, the nose geometry and the target material; it can be used to differentiate between thin and thick targets. They also found that for thick GRP targets less energy is absorbed for conical nosed projectiles showing they are more effective as penetrators, but the energy absorbed is essentially independent of the projectile nose geometry for thin GRP targets. Furthermore, they pointed out that when computing the work done to perforate a target all deformation mechanisms should be included. In their analysis the kinetic energy due to moving layers at the rear of the target and the ejected debris was ignored, as they required specialized instruments for characterization.

1.2. Constituents' properties

Various investigators [2,8–10] have delineated the effect of constituents' properties on failure modes. Whereas delamination and matrix cracking are influenced by matrix properties, fiber breakage depends upon fiber properties [8]. Attempts have been made to improve the delamination resistance of laminates by using thermoplastics and toughened polymer matrices. While these matrices increase the interlaminar strength of the laminate, they do not improve the damage resistance under extremely severe shock loads [2]. The matrix properties govern the damage threshold and the extent of impact damage while fiber properties govern the resistance to penetration [9]. Performance of composites when subjected to impact loads can be enhanced through improvements in the toughness of the resin systems; the toughness is a measure of material's ability to absorb strain energy, resist shear cracking and reduce effects of stress concentrations [8]. When every other parameter is kept constant, higher fiber strength provides better impact resistance [9].

1.3. Fiber length and fiber volume fraction

Fu et al. [10] studied effects of fiber volume fraction and fiber length on the energy absorbed during notched Charpy impact tests on both single (glass or carbon) and hybrid (glass and carbon) short-fiber-reinforced polypropylene (PP) composites. They attributed the increase in the fiber damage with an increase in the fiber volume fraction to the greater fiber-fiber interaction. It was found that the impact energy absorbed by the laminate increases with an increase in the glass fiber volume fraction, and decreases

with an increase in the carbon fiber volume fraction. This suggests that the cheaper glass fiber is more efficient in enhancing the fracture toughness of PP than the more expensive carbon fiber. Also, Morais et al. [7] found that glass fiber composites provided better resistance to compressive impact loads than carbon and aramid fibers; they attributed this to the fine structure of glass fibers and the resulting higher fiber/matrix contact area.

1.4. Fiber/matrix interface

For continuous fiber composites, the introduction of a material interface can increase the impact resistance of the composite [8]. Roy et al. [11] stated that a strong interfacial bond between the fiber and the resin matrix delayed the fiber/matrix debonding and longitudinal matrix cracking, and thus improved the overall performance of the composite. The strength of the interfacial bond can usually be enhanced by functionalizing fibers, i.e., coating them with a thin layer of suitable material prior to embedding them in the polymer matrix.

1.5. Ply stacking sequence

The ply stacking sequence in laminated composites has been shown to play an important role in the damage tolerance of composites [8]. Sjogren et al. [12] experimentally determined elastic properties of impact damaged carbon fiber/epoxy laminates. They found that the stiffness reduction of an impact damaged composite laminate is controlled mainly by the amount of fiber breakage, which depends upon the stacking sequence. Will et al. [5] experimentally studied the effect of the change in the laminate stacking sequence on its ability to dissipate kinetic energy of a projectile. The laminates were subjected to impacts up to and beyond their ballistic limits; the ballistic limit of a laminate equals the speed of a standard projectile at which it just perforates the target. The dominant energy dissipating mechanism was found to be delamination followed by shear fracture, and matrix cracking accounted for a small portion of the energy dissipated. Hull and Shi [13] proposed that delaminations are caused by interlaminar cracks. Since both transverse shear stresses and delaminations depend upon the laminate stacking sequence [14], therefore interlaminar cracks also depend on the stacking sequence [5]. The laminate stacking sequence influences the total delamination area, the delamination location, and the shear fracture area.

1.6. Impact energy

At low impact velocities, matrix cracking and delamination are usually the dominant damage processes. As the impact energy increases, the damaged area increases up to the ballistic limit when the damage tends to level off [15]. The total energy dissipated by material failure varies linearly with the impact energy up to the ballistic limit; however, it does not correlate well with the impact energy for impact speeds above the ballistic limit. Thus the ballistic limit is regarded as a threshold in the development of material damage [5]. Iannucci et al. [16] have stated that when the kinetic energy of a projectile is increased to ballistic levels, damage could result in through-the-thickness penetration and generally only local delaminations. The material at the impact site may additionally fail due to the localized shock created by the impact which suddenly raises the temperature of the material, and may induce a phase change. The residual compressive strength of the laminate was found to decrease indicating enhanced damage with an increase in the impact energy [15]. Shikhmanter et al. [17] studied the fractography of a quasi-isotropic tape first damaged by low energy level impacts and then loaded very slowly to failure in tension or compression. It was found that a distinction could be made between the damage caused by the impact, and that due to the two modes of subsequent loading.

Parga-Landa et al. [18] studied the effect of slamming pressure on the intralaminar behavior of composite panels by assuming that the slamming pressure can be modeled as a triangular pulse. When a wave crosses the boundary between layers of sharply different acoustic impedances, it is partially reflected and partially transmitted that may lead to strong shock wave dispersion causing loss of spall strength in some cases. Their analysis of the problem indicates that using properties of a homogenized material is not a good way to study dynamic loading of a heterogeneous body. Espinosa et al. [9] have suggested that dispersion effects may become more pronounced if voids are considered in the analysis.

1.7. Composite's heterogeneity

Espinosa et al. [9] have examined the effect of the waviness of fibers on the interlaminar shear failure of fiber reinforced plastics (FRPs) under impact loading. The fabrication of composites introduces waviness in the interface between adjoining laminas which may induce local shear stresses. Dandekar and Beaulieu's [19] experimental observations show that local shear stresses generated due to geometric heterogeneity of FRPs may cause delamination even under compressive loading.

1.8. Composite structures

Schonberg [20] investigated experimentally the impact resistance of several dual wall systems. A dual wall system is composed of an outer bumper that is subjected to impact loads, a pressure wall which is a layer on the exit side, and an inner layer between the two; there is empty space between every two adjoining layers. The laminate was used as one of the three layers in the dual wall system. Under equal impact energies, these systems performed no better than an aluminum dual wall system with each layer having the same specific strength. However, the composite used as

an inner layer or as a pressure wall provided greater protection to spacecraft occupants against damage caused by high-speed impacts.

1.9. Stitching composites

Mouritz [1,21] compared the damage resistance of stitched and unstitched GRP laminates loaded by an underwater shock wave produced by an explosion. The laminates were tested at low and high blast loads. It was found that unstitched and stitched laminates suffered the same types of damage that included cracking of the polymer matrix and glass fibers, small debonded lengths between the polymer and the glass fibers, and large delaminations between adjoining plies. However, the delaminated area was reduced by stitching with the greatest reduction occurring at a higher stitch density and when the stitches were along the fibers; it was attributed to stitching increasing the mode-I intralaminar fracture toughness. For ballistic projectiles, stitching slightly reduced the damage due to delamination of adjoining plies.

1.10. Boundary conditions

Boundary conditions at the edges of a composite laminate determine the tearing mechanism encountered [22], and noticeably affect the onset of failure and its subsequent propagation.

1.11. Remarks

Whereas most of the works cited above have ascertained the effect of only one parameter on the effectiveness of a composite laminate and have employed either numerical or experimental approaches, the present work provides the effect of various material and geometric parameters, and boundary conditions on the blast resistance of a composite laminate using the same mathematical model. Thus the sensitivity to different variables of the effectiveness of the composite in resisting blast loads can be easily delineated. However, because of space limitations, results for only a few cases are given.

There is extensive literature available on the impact response of composites, and only a few representative works are reviewed here. Inevitably, we have missed many relevant papers and even those containing more pertinent information. However, the above review provides, at least, a qualitative description of the effect of different parameters on the failure of composites under dynamic loads.

2. Problem formulation

We use the referential description of motion and rectangular Cartesian coordinates to describe lamina's deformations, and choose X_1-axis aligned along fibers, and X_2 and X_3 axes perpendicular to fibers; these are usually referred to as the material principal directions. Deformations are governed by the balance of mass, the balance of linear momentum, the balance of moment of momentum, and the balance of internal energy. These balance laws are supplemented by constitutive relations, initial conditions, and boundary conditions. We assume that the constitutive relation for the second Piola–Kirchhoff stress tensor $\boldsymbol{S}$ identically satisfies the balance of moment of momentum.

We use the theory of internal variables to describe damage evolution in rate dependent bodies. Let $\boldsymbol{\xi} = \{\phi^{\mathrm{m}}, \phi^{\mathrm{f}}, \phi^{\mathrm{d}}\}$ be the ordered set of three internal variables, and $\boldsymbol{\omega} = \{y^{\mathrm{m}}, y^{\mathrm{f}}, Y^{\mathrm{d}}\}$ the ordered set of corresponding conjugate forces. Referring the reader to [23] for details, we summarize here constitutive relations used in the present work. We assume that

$$\boldsymbol{S}(\boldsymbol{E}, \dot{\boldsymbol{E}}, \theta, \boldsymbol{G}, \boldsymbol{\xi}) = \boldsymbol{S}^{\mathrm{e}}(\boldsymbol{E}, \boldsymbol{0}, \theta, \boldsymbol{0}, \xi) + \boldsymbol{S}^{\mathrm{ne}}(\boldsymbol{E}, \dot{\boldsymbol{E}}, \theta, \boldsymbol{G}, \boldsymbol{\xi}), \quad (1)$$

and

$$\boldsymbol{\omega}(\boldsymbol{E}, \dot{\boldsymbol{E}}, \theta, \boldsymbol{G}, \boldsymbol{\xi}) = \boldsymbol{\omega}^{\mathrm{e}}(\boldsymbol{E}, 0, \theta, \boldsymbol{0}, \xi) + \boldsymbol{\omega}^{\mathrm{ne}}(\boldsymbol{E}, \dot{\boldsymbol{E}}, \theta, \boldsymbol{G}, \boldsymbol{\xi}), \quad (2)$$

where $\boldsymbol{S}^{\mathrm{e}}$ (equilibrium stress) denotes the value of the second Piola–Kirchhoff stress tensor $\boldsymbol{S}$ at zero strain rate and zero temperature gradient, and $\boldsymbol{\omega}^{\mathrm{e}}$ denotes the value of the conjugate force $\boldsymbol{\omega}$ at zero strain rate and zero temperature gradient. In Eqs. (1) and (2), $\boldsymbol{E}$, $\dot{\boldsymbol{E}}$, θ and $\boldsymbol{G}$ denote, respectively, the Green–St. Venant strain tensor, its rate, the temperature rise, and the temperature gradient. Henceforth, we consider isothermal processes; therefore, we do not consider the energy equation, and neglect effects of temperature rise and temperature gradient. Assuming that $\boldsymbol{S}^{\mathrm{e}}$ is an affine function of the strain tensor $\boldsymbol{E}$, it was shown in [23] that the equilibrium value of the conjugate force is given by Eq. $(3)_2$. That is,

$$S^{\mathrm{e}}_{\alpha\beta} = C^0_{\alpha\beta} + C_{\alpha\beta\gamma\delta}E_{\gamma\delta},$$
$$\omega^{\mathrm{e}}_{(i)} = Y^{e(i)} = \left(-\frac{\partial C^0_{\alpha\beta}}{\partial \phi^{(i)}}E_{\alpha\beta} - \frac{1}{2}\frac{\partial C_{\alpha\beta\gamma\delta}}{\partial \phi^{(i)}}E_{\alpha\beta}E_{\gamma\delta}\right), \quad i = m, f, d, \quad (3)$$

where $C^0_{\alpha\beta} = C^0_{\beta\alpha}$, $C_{\alpha\beta\gamma\delta} = C_{\gamma\delta\alpha\beta} = C_{\beta\alpha\gamma\delta}$, and these are functions of ξ. Eq. $(3)_1$ accounts for geometric nonlinearities and describes a neo-Hookean material with initial stress $\mathbf{C}^0$. We assume that a lamina reinforced with unidirectional fibers can be modeled as transversely isotropic with the axis of transverse isotropy perpendicular to the plane of the lamina. Thus there are five independent elastic constants out of the eighty-one components of $C_{\alpha\beta\gamma\delta}$. In terms of the more familiar elastic constants, components of matrix $[C]$ are given in Refs. [24–29]. Batra [30] has compared the response, in simple deformations, of four elastic materials whose constitutive relations account for geometric nonlinearities and the stress–strain relations are linear.

The matrix of elastic constants, the second Piola–Kirchhoff stress tensor, and the Green–St. Venant strain tensor are transformed to global coordinate axes by using tensor transformation rules [27,29].

Using the mechanics of materials approach to derive the dependence of material parameters upon damage variables [23], we get

$$E_1^{\mathrm{C}} = E_1^{\mathrm{f}} V^{\mathrm{f}} (1 - \phi^{\mathrm{f}}) + E_1^{\mathrm{m}} V^{\mathrm{m}}, \tag{4}$$

where E_1 is Young's modulus in the axial (or the fiber) direction; superscripts f and m signify quantities for the fiber and the matrix respectively, and V^{f} equals the volume fraction of the fiber. Furthermore, the effective axial Poisson's ratio v_{13}^{C} is found to be independent of the damage induced in the fiber and the matrix, and follows the rule of mixtures. Similarly, v_{12}^{C} is also given by the rule of mixtures, and is independent of the damage induced in the fiber and the matrix. The transverse modulus, E_2^{C}, is given by

$$\frac{1}{E_2^{\mathrm{C}}} = \frac{V^{\mathrm{f}}}{E_2^{\mathrm{f}}} + \frac{V^{\mathrm{m}}}{E_2^{\mathrm{m}}(1 - \phi^{\mathrm{m}})}, \tag{5}$$

and the effective shear modulus in the X_1X_2-plane by

$$\frac{1}{G_{12}^{\mathrm{C}}} = \frac{V^{\mathrm{f}}}{G_{12}^{\mathrm{f}}(1 - \phi^{\mathrm{d}})} + \frac{V^{\mathrm{m}}}{G_{12}^{\mathrm{m}}}. \tag{6}$$

The effective shear modulus in the X_2X_3-plane is taken to be independent of the debonding damage variable.

We note that as ϕ^{f} and ϕ^{m} approach 1.0, Young's moduli of the composite along and perpendicular to fibers approach, respectively, the axial Young's modulus of the matrix multiplied by the volume fraction of the matrix and zero. Similarly, in the limit of ϕ^{d} equaling 1.0, the shear modulus of the lamina in the X_1X_2-plane approaches zero. Thus at failure, material properties of the lamina have been severely degraded. Even though a damage variable affects only one of the elastic moduli in the material principal directions, it influences all moduli of the lamina when either global axes do not coincide with the material principal directions and/or applied tractions are not along the fibers.

2.1. Damage variables

We postulate that $\phi^{\mathrm{f}} = \phi^{\mathrm{f}}(Y^{\mathrm{f}})$, $\phi^{\mathrm{m}} = \phi^{\mathrm{m}}(Y^{\mathrm{m}})$, $\phi^{\mathrm{d}} = \phi^{\mathrm{d}}(Y^{\mathrm{d}})$, where the functional dependence is determined from the test data. It is assumed that the damage at a material point does not increase while the material there is unloading as indicated by a decrease in a suitable scalar measure of stresses and/or strains. Thus, the evolution of a damage variable is treated in a way analogous to that of incremental plastic strains for elastoplastic materials.

The composite material used for case studies is AS4/PEEK with $V^{\mathrm{f}} = 0.6$. Materials of the fiber and the matrix are assumed to be isotropic; values of their material parameters taken from Kyriakides et al. [31] and used in this work are given in Table 1. The least squares fit to the test data of Kyriakides et al. [31] gave the following expressions (see [23] for details)

Table 1
Values of material parameters of the fiber and the matrix[a]

	Matrix (PEEK)	Carbon fiber (AS4)
Poisson's ratio	0.356	0.263
Young's modulus (GPa)	6.14	214
Shear modulus (GPa)	2.264	84.7
Mass density (g/cm^3)	1.44	1.78

[a] The fiber and the matrix are assumed to be isotropic.

$$\phi^{\mathrm{f}} = A_{\mathrm{f}}(1 - e^{(-B_{\mathrm{f}} Y^{\mathrm{f}})}), \tag{7}$$

$$\phi^{\mathrm{m}} = \left(\frac{A_{\mathrm{m}} B_{\mathrm{m}} + C_{\mathrm{m}} (Y^{\mathrm{m}})^{D_{\mathrm{m}}}}{B_{\mathrm{m}} + (Y^{\mathrm{m}})^{D_{\mathrm{m}}}}\right), \tag{8}$$

$$\phi^{\mathrm{d}} = \left(\frac{A_{\mathrm{d}} B_{\mathrm{d}} + C_{\mathrm{d}} (Y^{\mathrm{d}})^{D_{\mathrm{d}}}}{B_{\mathrm{d}} + (Y^{\mathrm{d}})^{D_{\mathrm{d}}}}\right). \tag{9}$$

Values of constants A_{f}, B_{f}, A_{m}, B_{m}, C_{m}, D_{m}, A_{d}, B_{d}, C_{d}, and D_{d} are listed in Table 2. Constants in Eq. (7) expressing the damage variable due to fiber breakage have different values for tensile and compressive loading along the fiber direction. When fibers are not aligned with the loading axis, we first analyze the problem in the global coordinate system and then compute the normal strain along the fiber. The sign of E_{11} dictates which values of A_{f}, B_{f} and $Y_{\mathrm{crit}}^{\mathrm{f}}$ to use in Eq. (7). We follow a similar procedure for selecting appropriate values of A_{m}, B_{m}, C_{m}, D_{m} and $Y_{\mathrm{crit}}^{\mathrm{m}}$ in Eq. (8) and of A_{d}, B_{d}, C_{d}, D_{d} and $Y_{\mathrm{crit}}^{\mathrm{d}}$ in Eq. (9). In Table 2, $Y_{\mathrm{crit}}^{\mathrm{f}}$, $Y_{\mathrm{crit}}^{\mathrm{m}}$ and $Y_{\mathrm{crit}}^{\mathrm{d}}$ equal values of conjugate variables corresponding, respectively, to ϕ^{f}, ϕ^{m} and ϕ^{d} equaling 1.0, i.e., failure of the material point due to fiber breakage, matrix cracking and fiber/matrix debonding.

Table 2
Values of constants in Eqs. (7)–(11)

Damage properties		Tension	Compression
Fiber breakage	A_{f}	1.931 GPa	0.197 GPa
	B_{f}	1.931497	558
	$Y_{\mathrm{crit}}^{\mathrm{f}}$	0.0075 GPa	0.007535 GPa
Matrix cracking	A_{m}	1.356×10^{-10} GPa	0.01207 GPa
	B_{m}	0.00193	174
	C_{m}	0.37239 GPa	241 GPa
	D_{m}	0.43665	0.195
	$Y_{\mathrm{crit}}^{\mathrm{m}}$	0.0005 GPa	0.011 GPa
Fiber/matrix debonding	A_{d}	0.1437 GPa	
	B_{d}	0.00762	
	C_{d}	1.0022 GPa	
	D_{d}	0.37714	
	$Y_{\mathrm{crit}}^{\mathrm{d}}$	5.48×10^{-2} GPa	
Interfacial strength[a]	$[\sigma_{33}]$	0.078 GPa	
	$[\sigma_{13}]$	0.157 GPa	
	$[\sigma_{23}]$	0.157 GPa	

[a] Values for the ultimate interfacial strength were obtained from a composite data base site http://composite.about.com/library/data/blc-as4apc2-1.htm.

Even though ϕ^{f}, ϕ^{m} and ϕ^{d} depend only upon Y^{f}, Y^{m} and Y^{f} respectively, there is no restriction upon one damage mode influencing the evolution of other damage modes. Thus interaction among the four failure modes is implicitly considered. Also, at a given instant, different failure modes may ensue simultaneously at one or more points in the body.

2.2. Failure criterion

It is assumed that the failure due to fiber breakage, matrix cracking and fiber/matrix debonding occurs when $Y^{\mathrm{f}}, Y^{\mathrm{m}}$ and Y^{d} reach their critical values $Y^{\mathrm{f}}_{\mathrm{crit}}$, $Y^{\mathrm{m}}_{\mathrm{crit}}$ and $Y^{\mathrm{d}}_{\mathrm{crit}}$ respectively. Values of $Y^{\mathrm{f}}_{\mathrm{crit}}$, $Y^{\mathrm{m}}_{\mathrm{crit}}$ and $Y^{\mathrm{d}}_{\mathrm{crit}}$ depend upon materials of the fiber and the matrix, sizing of fibers, and possibly on the fabrication process; these are to be determined from the experimental data. Values for the AS4/PEEK composite found from the test data [31] and used herein are listed in Table 2.

In order to simulate the delamination behavior, cracks are allowed to propagate in an interface between adjoining laminae. A perfect bond is assumed between the adjoining laminae until a damage surface, defined by

$$D_{\mathrm{d}} = \left(\frac{\sigma_{33}}{[\sigma_{33}]}\right)^2 + \left(\frac{\sigma_{13}}{[\sigma_{13}]}\right)^2 + \left(\frac{\sigma_{23}}{[\sigma_{23}]}\right)^2 = 1 \quad (\sigma_{33} \geqslant 0), \tag{10}$$

is reached. Here $[x]$ denotes the ultimate value of the quantity x, and $\boldsymbol{\sigma}$ the Cauchy stress tensor. The failure envelope (10) depends on the transverse normal and the transverse shear stresses at the lamina's interface. When stresses at a point(s) on the interface satisfy Eq. (10), the adjoining layers are allowed to separate there. However, when $\sigma_{33} < 0$, the failure envelope (10) is modified to

$$D_{\mathrm{d}} = \left(\frac{\sigma_{13}}{[\sigma_{13}]}\right)^2 + \left(\frac{\sigma_{23}}{[\sigma_{23}]}\right)^2 = 1 \quad (\sigma_{33} < 0). \tag{11}$$

In this case there is no separation of adjoining plies but there is relative sliding between points on the two sides of the contacting surface. We have listed in Table 2 values of ultimate strengths $[\sigma_{33}]$, $[\sigma_{13}]$ and $[\sigma_{23}]$. We note that the failure envelope corresponds to mode-II failure. For $\sigma_{13} = \sigma_{23} = 0$, Eq. (10) represents mode-I failure. For the mode-I failure, newly created surfaces are taken to be traction free, and points on them are checked for non-interpretation during subsequent deformations.

2.3. Strain rate effect

We postulate the following functional dependence of conjugate damage variables Y^{m} and Y^{d} upon $\dot{E}_{22}$ and $\dot{\gamma}_{12}$ respectively:

$$Y^{\mathrm{m}} = \left(\frac{B_{\mathrm{m}}\left(-A_{\mathrm{m}} + \phi^{\mathrm{m}}\left(1 - s^{\mathrm{m}}\log_{10}\left(\frac{\dot{E}_{22}}{\dot{E}^0_{22}}\right)\right)\right)}{C_{\mathrm{m}} - \phi^{\mathrm{m}}\left(1 - s^{\mathrm{m}}\log_{10}\left(\frac{\dot{E}_{22}}{\dot{E}^0_{22}}\right)\right)}\right)^{1/D_{\mathrm{m}}}, \tag{12}$$

$$Y^{\mathrm{d}} = \left(\frac{B_{\mathrm{d}}\left(-A_{\mathrm{d}} + \phi^{\mathrm{d}}\left(1 - s^{\mathrm{d}}\log_{10}\left(\frac{\dot{E}_{12}}{\dot{E}^0_{12}}\right)\right)\right)}{C_{\mathrm{d}} - \phi^{\mathrm{d}}\left(1 - s^{\mathrm{d}}\log_{10}\left(\frac{\dot{E}_{12}}{\dot{E}^0_{12}}\right)\right)}\right)^{1/D_{\mathrm{d}}}. \tag{13}$$

Here $\dot{E}^0_{22}$ and $\dot{E}^0_{12}$ represent, respectively, values of the reference transverse and the reference shear strain rates. Y^{f} is assumed to be independent of strain rate because the experimental stress–strain curve for AS4/PEEK in longitudinal tension and compression is insensitive to the axial strain rate.

Using Vogler and Kyriakides's [32] test data for transverse compression and in-plane shear, the value of the material parameters s^{m} is determined by plotting $\left(1 - s^{\mathrm{m}}\log_{10}\left(\frac{\dot{E}_{22}}{\dot{E}^0_{22}}\right)\right)$ versus ϕ^{m} at $Y^{\mathrm{m}} = 0.006$ and setting the reference transverse strain rate, $\dot{E}^0_{22}$, equal to 1.6×10^{-5}/s. It is found that the least squares fit to the data points is a straight line passing through the origin, and its slope, 0.0361, equals s^{m}. A similar procedure gives the value 0.0013 of the material constant s^{d}; in this case the data is plotted for $Y^{\mathrm{d}} = 0.03$ and the reference shear strain rate, $\dot{E}^0_{12}$, equals 1×10^{-5}/s. The material constant, Y^i_{crit} $(i = \mathrm{f}, \mathrm{m}, \mathrm{d})$, was assumed to be strain rate independent because failure strains reported in Vogler and Kyriakides [32] do not exhibit any clear dependency upon the strain rate. Similarly, for a lack of test data, the interfacial strengths $[\sigma_{33}]$, $[\sigma_{13}]$ and $[\sigma_{23}]$ of the composite are assumed to be strain rate independent.

3. Mathematical model

3.1. Governing equations

Substitution from Eq. (3) into the balance of linear momentum gives the following nonlinear field equation for the determination of the displacement $\mathbf{u}$.

$$\rho_R \ddot{u}_i = [(\delta_{i\alpha} + u_{i,\alpha})(C_{\alpha\beta\gamma\delta}E_{\gamma\delta})]_{,\beta} + \rho_R b_i, \tag{14}$$

where we have assumed that the material in the reference configuration is stress free. In the total Lagrangian description of motion, the independent variables are places $\mathbf{X}$ and time t, and the dependent variables are $\mathbf{x}$ or $\mathbf{u}$ since knowing $\mathbf{x}$, the present mass density can be computed from the balance of mass. Let Ω be the region occupied by the body in the reference configuration at time $t = 0$. A general form of initial and boundary conditions is

$$\begin{aligned} &x_i(\mathbf{X}, 0) = X_\alpha \delta_{i\alpha}, \\ &\dot{x}_i(\mathbf{X}, 0) = v^0_i(\mathbf{X}), \\ &x_i(\mathbf{X}, t) = \bar{x}_i(\mathbf{X}, t), \quad \mathbf{X} \in \partial_{\mathbf{X}}\Omega, \quad t \in (0, \widetilde{T}), \\ &T_{i\alpha}(\mathbf{X}, t)N_\alpha(\mathbf{X}) = f_i(\mathbf{X}, t), \quad \mathbf{X} \in \partial_f\Omega, \quad t \in (0, \widetilde{T}). \end{aligned} \tag{15}$$

Here $\partial_{\mathbf{X}}\Omega$ and $\partial_f\Omega$ are parts of the boundary $\partial\Omega$ of Ω where final positions (or equivalently, displacements) and surface tractions are prescribed, respectively, as $\boldsymbol{x}$ and $\boldsymbol{f}$, and $\mathbf{T}$ is the first Piola–Kirchhoff stress tensor. Note that $\partial_X\Omega$ and $\partial_f\Omega$ need not be disjoint since linearly independent

components of displacements and surface tractions may be specified at the same point on $\partial\Omega$. However, for the sake of simplicity, they are assumed to be disjoint in Eq. (15). Initial values of internal variables representing the fiber breakage, fiber/matrix debonding, and matrix cracking are taken to be zeros.

Because of the dependence of elastic constants upon the damage variables, material properties change as the composite is deformed.

3.2. Numerical solution

A weak form of Eq. (14) is derived by using the Galerkin approximation; e.g. see Hughes [33]. It reduces nonlinear partial differential Eq. (14) to nonlinear ordinary differential equations (ODEs), which are integrated with respect to time t by using the subroutine LSODE (Livermore Solver for Ordinary Differential Equations) that adaptively adjusts the time step size in order to compute the solution within the prescribed accuracy.

A 3-D finite element (FE) code based on the afore-stated problem formulation has been developed in Fortran. Degrees of freedom at each node are three components of displacement, and three components of velocity since LSODE integrates first order ODEs. The code employs 8-node brick elements. Various domain integrals involving integration on an element Ω_e that appear in the weak formulation of the problem are evaluated by using the $2\times2\times2$ Gauss quadrature rule. During the time integration of the coupled ODEs, absolute and relative error tolerances in LSODE were each set equal to 1×10^{-9}, and MF was assigned the value 10. The parameter MF determines the integration method in LSODE, and MF = 10 implies the use of the Adam–Moulton method. After having found nodal displacements, values of conjugate variables and damage parameters (or internal variables) ϕ^f, ϕ^m and ϕ^d at each integration point are determined, and are used to update elastic constants for computing results at the next time step.

3.3. Simulation of material failure

When an internal variable ϕ^f, ϕ^m and/or ϕ^d equals 1.0 or the corresponding conjugate variable Y^f, Y^m and/or Y^d equals its critical value, then the material there is taken to have failed due to fiber breakage, matrix cracking and/or fiber/matrix debonding respectively. Even if the material at all eight integration points within an element has failed, that element is not removed from the analysis. Once all elastic constants at each one of the eight integration points in an element have been reduced to zero, all stress components in that element will subsequently be zero, and for all practical purposes that element will represent a hole or a void.

In order to simulate either sliding or crack initiation and propagation due to delamination, we assume that when the stress state at a node N has reaches the failure envelope represented by Eqs. (10) and (11), an additional node N^* coincident with N but not connected to it is added there. The nodal connectivity of elements sharing the node N is modified in the sense that one or more of these elements is now connected to the newly added node N^* rather than the node N. However, no new element is created in this process. We note that delamination may ensue simultaneously at several nodes. If subsequent deformations of the body move nodes N and N^* apart and create new surfaces, then these surfaces are taken to be traction free. The non-interpenetration of nodes N and N^* into the material is avoided by connecting these two nodes with a 1-D two-node spring element that is weak in tension but stiff in compression. The constitutive relation for the stiff spring is taken to be

$$F = kz_n,$$

where

$$k = \begin{cases} 0, & z_n/z_0 \geqslant 0, \\ E_3 l\left[1+(\eta E_3-1)\left(\dfrac{z_n}{z_0}\right)^2\right], & -1 \leqslant z_n/z_0 < 0, \\ \eta E_3 l, & z_n/z_0 < -1. \end{cases} \quad (16)$$

Here F is the normal force between nodes N and N^*, E_3 Young's modulus of the composite in the X_3-direction, z_n the relative displacement between nodes N and N^* normal to the interface, l a characteristic length, and η a constant.

3.4. Verification of the code

As described in [23] the code was verified by using the method of fictitious body forces. Also, computed results for simple problems such as wave propagation in a bar were compared with their analytical solutions. It ensures that the code gives an accurate numerical solution of the governing equations.

3.5. Validation of the mathematical model

Referring the reader to [23] for details, we note that values of material parameters for the AS4/PEEK composite were derived from the test data of Kyriakides et al. [31]. Subsequently, computed results were compared with experimental observations of different investigators and under totally different loading configurations. The close agreement between computed results and test findings validated the mathematical model.

4. Brief description of the analysis technique

The 3-D FE code, with strain rate dependent damage evolution equations, is used to numerically investigate the damage induced in fiber reinforced composite marine structures due to underwater explosive shock loads. The effect, if any, of temperature changes on structure's response has been neglected, and a mechanical problem has been ana-

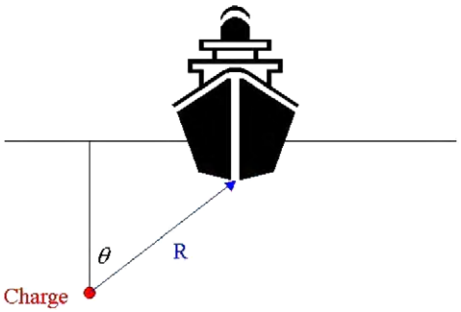

Fig. 1. Schematic of a ship structure subjected to an underwater explosive load.

lyzed. Fig. 1 schematically depicts a ship structure subjected to a blast load due to an explosive charge W (kg) positioned at a stand-off distance, R (m), and an angle, θ, from the ship structure. A 10 mm thick, 220 mm × 220 mm square, AS4/PEEK composite panel with the fiber volume fraction, V^f, of 0.6 is considered for the analysis. These dimensions were chosen to match with those of the test specimen used by Turkmen and Mecitolu [34] who studied the dynamic response of a laminated composite subjected to air blast loads, and are of the same order of magnitude as those employed in other tests; e.g., Comtois et al. [35] used a 216 mm diameter, 2.1 mm thick circular plate, Langdon et al. [36] a 220 mm × 220 mm × (1.6–2.62 mm) plate, and Mouritz [1] a 270 mm × 70 mm × 6.1 mm rectangular plate. Mechanical properties of the fiber and the matrix are given in Table 1, and values of parameters in damage relations (7)–(11) in Table 2.

Fig. 2 is a schematic sketch of the problem analyzed. The panel is made of four plies, and is divided into 8-noded brick elements with finer elements in the central portion. All four edge surfaces of the specimen are fixed; i.e., $u_1 = u_2 = u_3 = 0$ on surfaces $X_1 = 0$, $X_1 = 220$ mm, $X_2 = 0$, and $X_2 = 220$ mm. A FE discretization of the domain is exhibited in Fig. 3 with smaller elements near the center of the panel and coarser elements elsewhere. The load due to underwater explosion is simulated by applying a time-dependent pressure field on the top surface of the specimen; the pressure also varies with the distance, r, from the centroid of the top surface of the panel. The peak pressure is assumed to occur at $r = 0$, and decrease

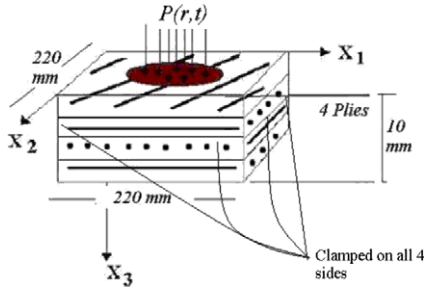

Fig. 2. Schematic sketch of the problem analyzed.

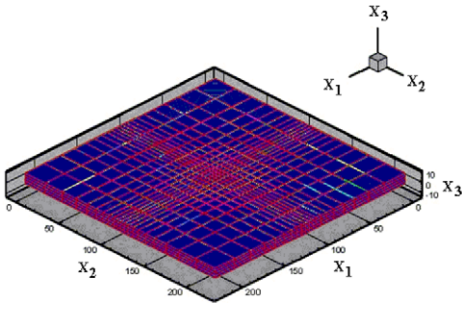

Fig. 3. Discretization of the panel into a FE mesh of $20 \times 20 \times 4$ elements.

exponentially with the passage of time as given by Cole [37].

$$P(t) = P_{\max} e^{-t/\lambda}. \tag{17}$$

In Eq. (17), $P_{\max}$ is the peak pressure in the shock front, t the time elapsed since the arrival of the shock wave, and λ the decay time constant. The peak pressure, $P_{\max}$, and the decay constant, λ, are given by

$$P_{\max} = K_1 \left(\frac{W^{1/3}}{R}\right)^{A_1}, \tag{18}$$

$$\lambda = K_2 W^{1/3} \left(\frac{W^{1/3}}{R}\right)^{A_2}, \tag{19}$$

where constants K_1, K_2, A_1 and A_2 depend upon the explosive charge; their values for four explosives, taken from Liang and Tai [38], are listed in Table 3. Fig. 4 exhibits a typical pressure–time variation at $r = 0$.

Turkmen and Mecitolu [34] experimentally analyzed the dynamic response of a stiffened laminated composite plate subjected to air-blast loading. They also studied the effect

Table 3
Values of constants in Eqs. (18) and (19) for various explosives [36]

Explosive type	TNT	HBX-1	PETN	Nuclear
K_1	52.12	53.51	56.21	1.06×10^4
A_1	1.18	1.144	1.194	1.13
K_2	0.0895	0.092	0.086	3.627
A_2	−0.185	−0.247	−0.257	−0.22

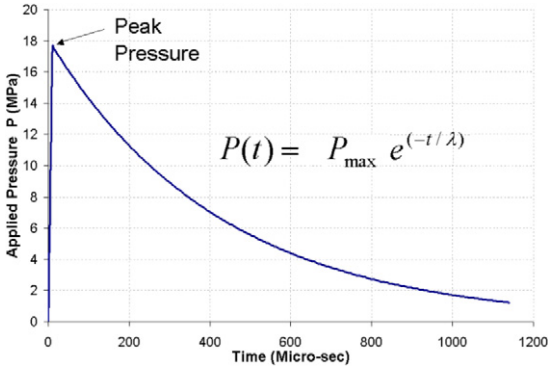

Fig. 4. Variation at $r = 0$ of pressure with time for TNT explosive with $W = 64$ kg and $R = 10$ m.

the distance, R, between the charge and the target has on the pressure distribution over the specimen. For large values of R, the shock wave is planar and the pressure distribution on the specimen is nearly uniform. However, we consider here the case of the pressure being non-uniform over the specimen with its peak value occurring at the centroid of the impacted surface. The polynomial function obtained by using a least squares fit to the pressure distribution over the 220 mm × 220 mm specimen found by Turkmen and Mecitolu [34] is

$$P(r,t) = (-0.0005r^4 + 0.01r^3 - 0.0586r^2 - 0.001r + 1)P(t), \tag{20}$$

where r is the distance, in cm, from the specimen center. For a fixed value of time t, Fig. 5 shows the variation of the pressure with r. We have tacitly assumed here that the spatial variation of the pressure exerted on a flat plate by a shock wave traveling in water and in air is the same.

The shock factor is a measure of the severity of the attack, and relates the charge weight to the distance between the point of ignition and the target plate; the shock wave pressure varies with the charge weight, the standoff distance, and the relative attack orientation. A higher value of the shock factor implies that a larger portion of energy of the underwater explosion is imparted to the ship. For submarines, this factor is called the Hull Shock Factor (HSF) [39,40], and is given by

$$\text{HSF} = \left(\frac{W^{1/2}}{R}\right). \tag{21}$$

For a surface ship, it is necessary to correct Eq. (21) for the angle at which the shock wave strikes the target; the corrected value, termed the Keel Shock Factor (KSF) [39], is given by

$$\text{KSF} = \left(\frac{W^{1/2}}{R}\right)\left(\frac{1+\cos(\theta)}{2}\right). \tag{22}$$

In order to assess structure's resistance to impact loads, the following quantities are computed: work done due to applied loads by Eq. (23); energies dissipated due to fiber breakage, matrix cracking, fiber/matrix debonding, and delamination via Eqs. (24)–(26) and (29) respectively; work done to deform the body via Eq. (27), and the kinetic energy of the body at the terminal value of the time t via Eq. (28).

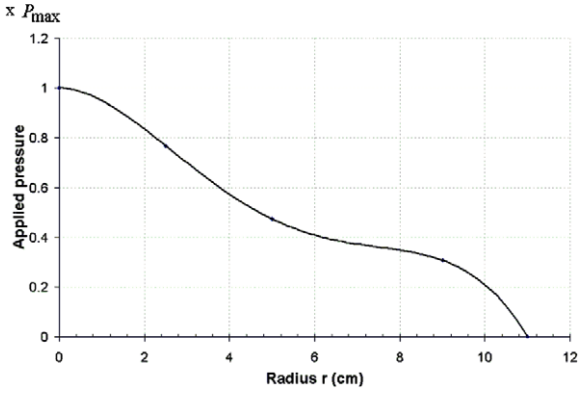

Fig. 5. For a fixed value of time t, pressure distribution over the specimen's top surface.

$$\text{Work done by external forces} = \int_0^t \sum_n F_3^n \frac{\mathrm{d}u_3^n}{\mathrm{d}t}\,\mathrm{d}t. \tag{23}$$

The summation is Eq. (23) is over all nodes on the top surface of the laminate where pressure is applied.

Energy dissipated due to fiber breakage

$$= \int_0^t \int_V Y^{\mathrm{f}} \frac{\mathrm{d}\phi^{\mathrm{f}}}{\mathrm{d}t}\,\mathrm{d}V\,\mathrm{d}t = \int_0^{\phi^f} \int_V Y^{\mathrm{f}}\,\mathrm{d}\phi^{\mathrm{f}}\,\mathrm{d}V, \tag{24}$$

Energy dissipated due to matrix cracking

$$= \int_0^t \int_V Y^{\mathrm{m}} \frac{\mathrm{d}\phi^{\mathrm{m}}}{\mathrm{d}t}\,\mathrm{d}V\,\mathrm{d}t = \int_0^{\phi^{\mathrm{m}}} \int_V Y^{\mathrm{m}}\,\mathrm{d}\phi^{\mathrm{m}}\,\mathrm{d}V, \tag{25}$$

Energy dissipated due to fiber/matrix debonding

$$= \int_0^t \int_V Y^{\mathrm{d}} \frac{\mathrm{d}\phi^{\mathrm{d}}}{\mathrm{d}t}\,\mathrm{d}V\,\mathrm{d}t = \int_0^{\phi^{\mathrm{d}}} \int_V Y^{\mathrm{d}}\,\mathrm{d}\phi^{\mathrm{d}}\,\mathrm{d}V, \tag{26}$$

Work done to deform the body

$$= \int_0^t \int_V S_{\alpha\beta} \frac{\mathrm{d}E_{\alpha\beta}}{\mathrm{d}t}\,\mathrm{d}V\,\mathrm{d}t. \tag{27}$$

$$\text{Kinetic energy} = \int_V \frac{\rho}{2}(v_x^2 + v_y^2 + v_z^2)\,\mathrm{d}V, \tag{28}$$

Energy dissipated in delamination

= Work done by external forces

– Work done to deform the body – Kinetic energy

– Energy dissipated due to other three failure modes. (29)

Eq. (29) follows from the balance of energy.

5. Results and discussion

The AS4/PEEK composites studied here failed at an effective strain between 1% and 2%. For such small deformations, all three stress tensors, namely the first Piola–Kirchhoff, the second Piola–Kirchhoff and the Cauchy, are essentially equal to each other. Results presented below in terms of components of the second Piola–Kirchhoff stress tensor can also be interpreted in terms of the other two stress tensors.

5.1. Effect of the finite element mesh

For one loading, the following four meshes were considered: 20 × 20 × 4 (1600 elements, 2205 nodes), 20 × 20 × 8 (3200 elements, 3969 nodes), 40 × 40 × 4 (6400 elements, 8405 nodes), and 40 × 40 × 8 (12,800 elements, 15,129 nodes), with each mesh being fine in the central portion of the specimen; e.g. see Fig. 3. These are identified as meshes 1, 2, 3 and 4 in Fig. 6. For $W = 64$ kg of TNT

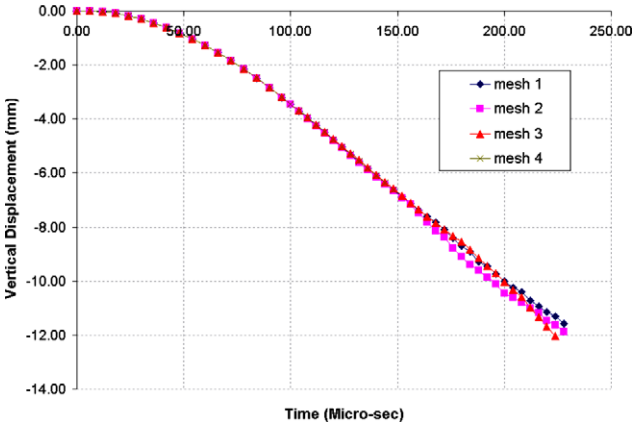

Fig. 6. For the four meshes, time histories of the vertical displacement of the specimen centroid ($X_1 = 110$ mm, $X_2 = 110$ mm, and $X_3 = 5$ mm).

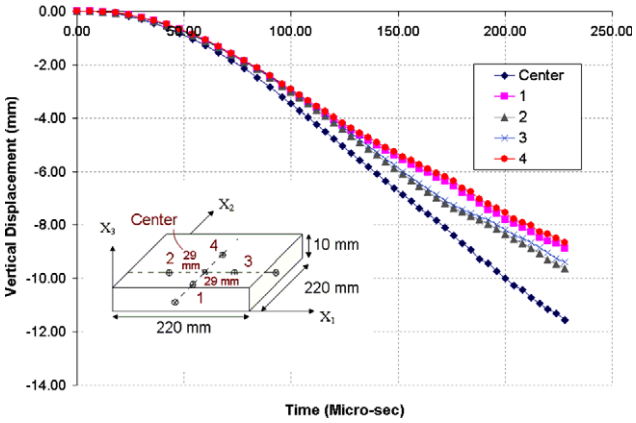

Fig. 7. Time histories of vertical displacements of five different points of the mid-surface $X_3 = 5$ mm with fibers oriented along the X_1-axis.

explosive, and $R = 10$ m, P_{max} was calculated from Eq. (18) and its spatial distribution over the top surface from Eq. (20). Computations were stopped at 230 μs, since then each one of the three damage variables had reached 1.0 at the centroid of the laminate. For the four meshes, Fig. 6 shows time histories of the vertical displacement of the specimen centroid located at $X_1 = 110$ mm, $X_2 = 110$ mm, and $X_3 = 5$ mm. It is clear that the maximum difference in the centroidal displacement computed with any two meshes is about 4.8%. At 152 μs, the maximum of the tensile principal stresses at all nodes equaled 1.39331, 1.32323, 1.23361, and 1.24554 GPa, for meshes 1, 2, 3, and 4, respectively, while that in compression equaled −0.885363, −0.893707, −0.916503, −1.02709 GPa. The maximum percentage difference is about 11% for the tensile principal stresses, and 13.7% for the compressive ones. The work done to deform the body, calculated using Eq. (27) was found to be 378.13, 408.19, 397.91 and 405.15 J, respectively, for meshes 1, 2, 3, and 4. The maximum difference in these four values is about 7%. Thus, we will use the $20 \times 20 \times 4$ elements mesh for the remaining analyses in order to save on computational resources. It will help identify quickly variables to which the impact damage is most sensitive. If desired, subsequent computations can be performed with a finer mesh to obtain improved results.

5.2. Fiber orientation

In order to examine the effect of the fiber orientation on the impact resistance of the composite structure all four plies were assumed to have the same fiber orientation, and seven different fiber orientations, θ, namely, $\theta = 0°$, 10°, 30°, 45°, 60°, 75° and 90°, were considered. We first present results for $\theta = 0°$. Fig. 7 exhibits time histories of the vertical displacement of five points of the mid-surface $X_3 = 5$ mm; locations of these points are depicted in the Fig. inset. As expected, the maximum deflection occurs at specimen's centroid. Note that the applied pressure has the highest value at the centroid of the top surface. Vertical

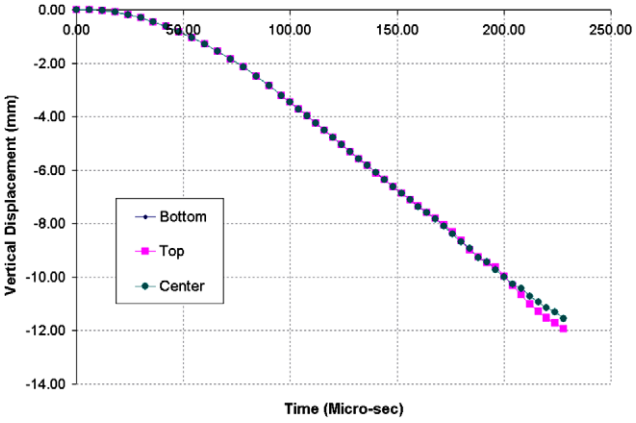

Fig. 8. Time histories of the vertical displacements of the centroids of planes $X_3 = 0$ (bottom), $X_3 = 5$ mm (center), and $X_3 = 10$ mm (top) with fibers oriented along the X_1-axis.

displacements at locations 2 and 3 are nearly the same, and those at points 1 and 4 are essentially equal to each other, but deflections at points 2 and 3 are higher than those at points 1 and 4; this difference is attributed to fibers being oriented along the X_1-axis. Although the body is assumed to be initially homogeneous, the difference in the evolution of damage along the X_1 and the X_2 directions, and the dependence of material properties upon the damage evolved annihilates the uniformity of material properties. It is evident from time histories of vertical displacements at centroids of planes $X_3 = 0$ (bottom surface), $X_3 = 5$ mm (mid-surface), and $X_3 = 10$ mm (top surface) exhibited in Fig. 8 that the vertical displacements at these three points are very close to each other primarily because of the high speed of elastic waves in the transverse direction and very small laminate thickness.

5.2.1. Fiber/matrix debonding

Fig. 9 depicts evolution of the fiber/matrix debonding at the same five points where time histories of evolution of the vertical displacement were plotted in Fig. 7. The two plots

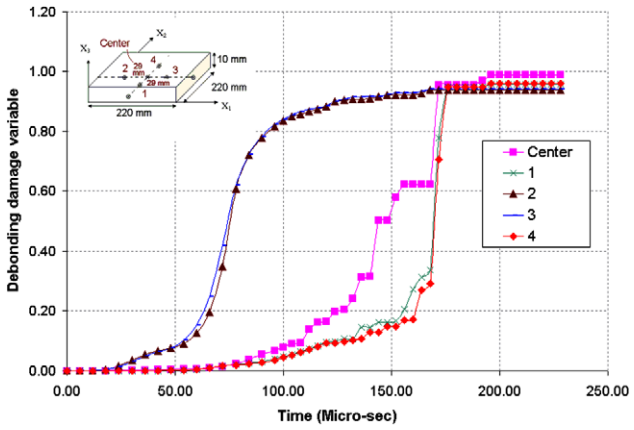

Fig. 9. Time histories of evolution of the debonding damage variable at the five points on specimen's mid-surface with fibers oriented along the X_1-axis.

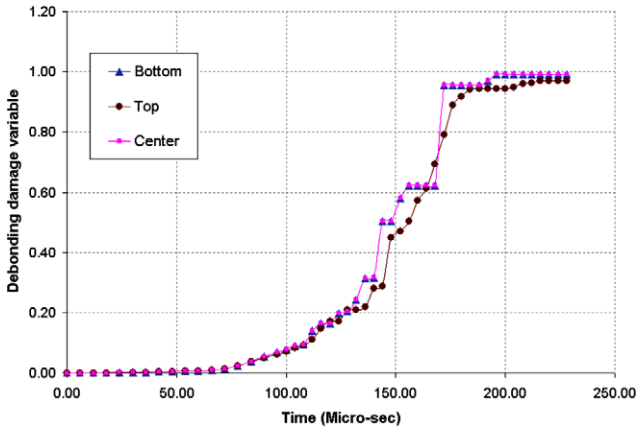

Fig. 11. Time histories of evolution of the debonding damage variable at centroids of planes $X_3 = 0$ (bottom), $X_3 = 5$ mm (center), and $X_3 = 10$ mm (top) with fibers oriented along the X_1-axis.

are qualitatively similar in the sense that, at any time, damages evolved at points 1 and 4 are nearly the same, and those at points 2 and 3 are close to each other. Furthermore, the damage begins to evolve sooner at points 2 and 3 than at points 1 and 4, and its rate of growth is also higher at points 2 and 3 than that at points 2 and 4. This is reasonable because debonding between fibers and the matrix occurs along fibers rather than in a direction perpendicular to fibers. The debonding damage variable at the specimen centroid does not equal the average of those at points 1 through 4.

One can conclude from fringe plots of the debonding damage variable at four different times, shown in Fig. 10, that the debonding starts from edges perpendicular to the fibers and propagates, along the fibers, towards the center.

Fig. 11 represents time histories of evolution of the debonding damage variable at centroids of the top, the middle, and the bottom surfaces of the laminate. It is clear that at any time t, values of the debonding damage variable at these three points are nearly the same implying that debonding propagates in the thickness direction instantaneously.

At $t = 160$ μs, Fig. 12 exhibits fringe plots of the debonding damage variable, the Fig. on the left depicts the damage distribution on the top surface, and that on the right the damage distribution on the bottom surface. It is evident that damage distributions on the top and the bottom surfaces are nearly identical to each other because of the small thickness of the laminate. It does not take much time for the loading wave to propagate through the laminate thickness. Fringe plots of the in-plane shear stress S_{12} are evinced in Fig. 13, and those of the transverse shear stress S_{13} in Fig. 14. The maximum magnitude of S_{12} occurs at centroids of regions in the four quadrants, the shear stress is positive at points in the first and the third quadrants, and negative at points in the second and the fourth quadrants. The in-plane shear stress is nearly zero in the central portion of the specimen. We conclude from fringe plots of Fig. 14 that the maximum magnitude of the transverse shear stress S_{13} occurs at points on the edges $X_1 = 0$ and $X_1 = 220$ mm where delamination initiated. The magnitude of the shear stress is nearly symmetrical about the mid-surface with positive values occurring at points above it, and negative values at points below it. The maximum magnitudes of the in-plane and the transverse shear stresses are nearly equal to each other even though they occur at different points.

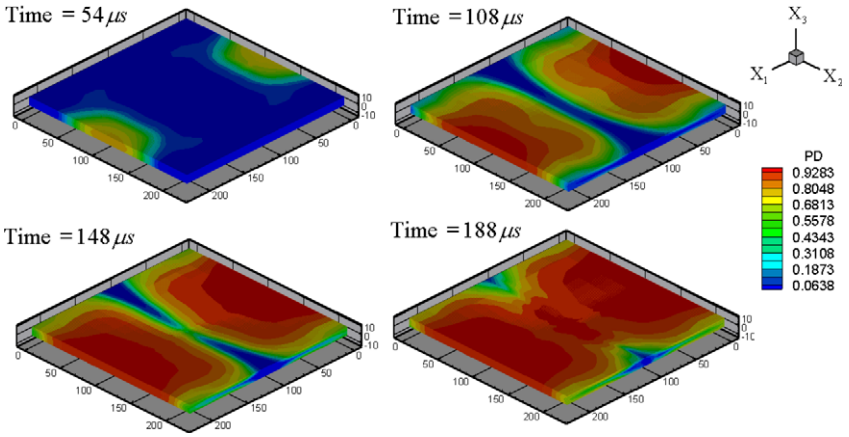

Fig. 10. Fringe plots of the debonding damage variable at four different times; PD stands for the debonding damage variable.

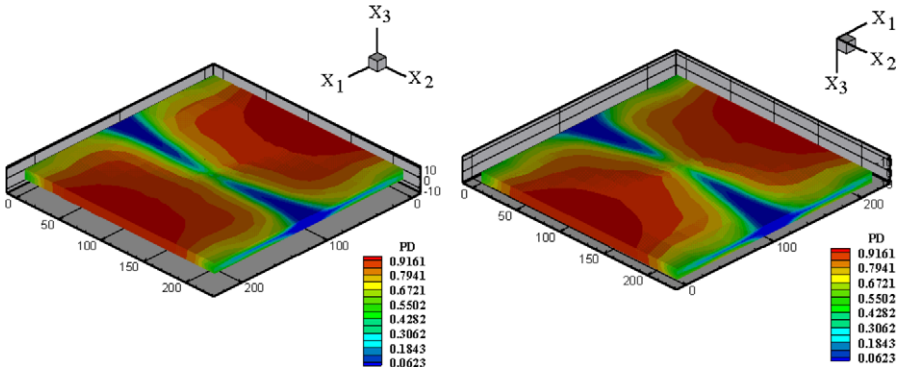

Fig. 12. Fringe plots of the debonding damage variable in the specimen at $t = 160$ μs; left: top surface; right: bottom surface.

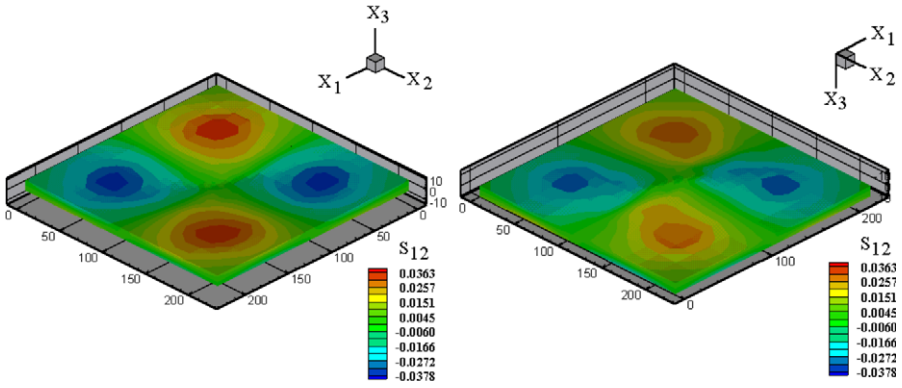

Fig. 13. Fringe plots of the shear stress (GPa), S_{12}, in the specimen at $t = 160$ μs; left: top surface; right: bottom surface.

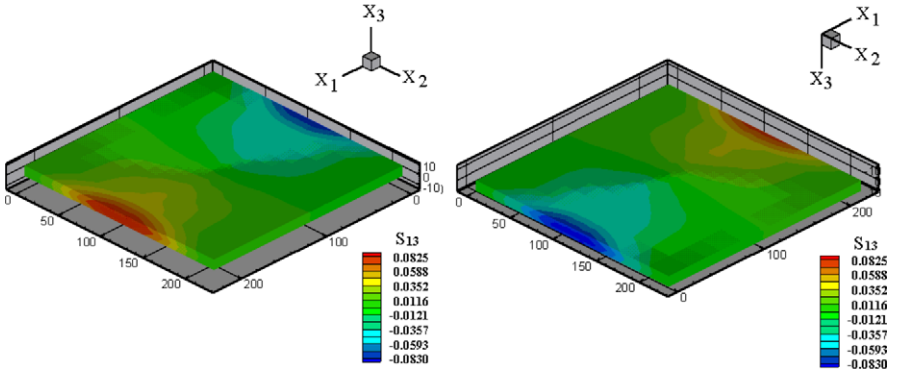

Fig. 14. Fringe plots of the shear stress (GPa), S_{13}, in the specimen at $t = 160$ μs; left: top surface; bottom: right surface.

5.2.2. Matrix cracking

Fringe plots of the matrix cracking damage variable, at four times, given in Fig. 15 show that the matrix cracking begins at about 108 μs at the centroid of the bottom surface; it propagates faster along fibers (i.e., X_1-axis) than in the transverse direction (i.e., X_2-axis). This agrees qualitatively with Luo et al.'s [41] results who observed, in their experiments, that matrix cracks propagated along fibers in the bottom-most layer.

Time histories of evolution of the matrix cracking damage variable at five points on specimen's mid-surface, exhibited in Fig. 16, reveal that the matrix cracking begins rapidly at specimen's centroid at about 125 μs, and the matrix at all five points considered has cracked when $t = 170$ μs. It instantaneously increases from 0.3 to 1.0 indicating that the matrix cracks suddenly rather than gradually; it is a characteristic of the damage evolution Eq. (8). Fringe plots of Fig. 15 signify that the cracked region in the bottom surface is not circular even though the loaded region on the top surface is circular.

Fringe plots of Fig. 17 reveal that matrix cracking on the top surface ensues from points on clamped edges that are also on the planes $X_2 = 0$, 200 mm, and propagates inwards. Furthermore, at least at time $t = 160$ μs, the shape and the size of the cracked matrix region in the top surface is quite different from that in the bottom surface; this

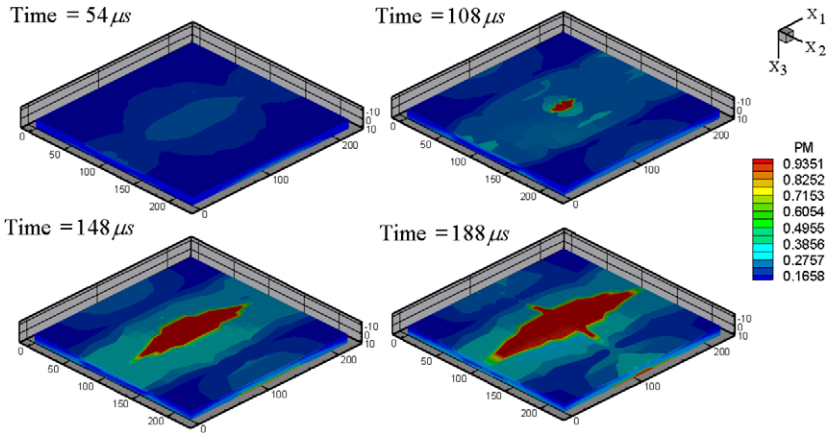

Fig. 15. Fringe plots of the matrix cracking damage variable at four times; PM stands for the matrix cracking damage variable.

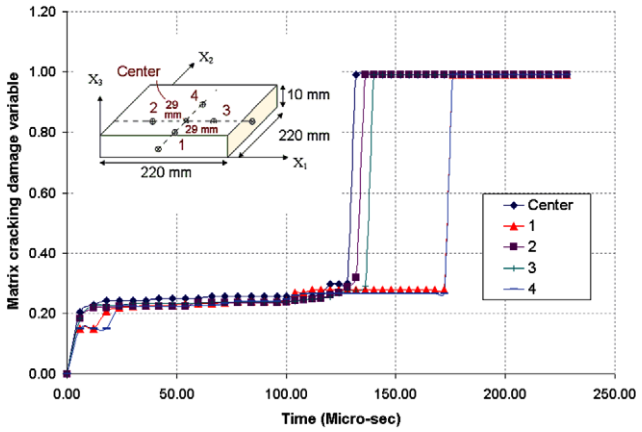

Fig. 16. Time history of evolution of the matrix cracking damage variable at five points on specimen's mid-surface with fibers oriented along the X_1-axis.

region is centered about the X_2-axis on the top surface but around the centroid in the bottom surface. Fig. 18 exhibits at time $t = 100$ μs fringe plots of the normal stress S_{22}; the stress distributions around the centroids of the top and the bottom surfaces are nearly identical except that it is compressive at points on the top surface, and tensile at points on the bottom surface. The magnitudes of the normal stress at corresponding points on the top and the bottom surfaces are nearly the same. On the top surface, large positive values of S_{22} also occur at points near the edges that are close to the X_2-axis. Time histories of evolution of the matrix cracking damage variable at centroids of the top, the middle, and the bottom surfaces, plotted in Fig. 19, imply that the matrix cracks simultaneously and instantaneously at the centroids of the bottom and the middle surfaces but much later at the centroid of the top surface because of S_{22} being tensile at points on the bottom surface and compressive at points on the top surface. Our results agree qualitatively with Mouritz's [3] experimental observations of cracking of the polymer matrix on the back surface of the laminate; Mouritz [3] attributed it to high tensile bending stresses developed there. One reason for matrix cracking to initiate first at the bottom surface is that a compressive wave is reflected from there as a tensile wave which can induce more damage. Also, the spalling failure mode could ensue at points on the bottom surface, but it is not considered here.

5.2.3. Fiber breakage

Figs. 20 and 21 depict, respectively, fringe plots of the fiber breakage damage variable at four times, and time histories of evolution of the fiber breakage damage variable at five points on specimen's mid-surface. They reveal that the

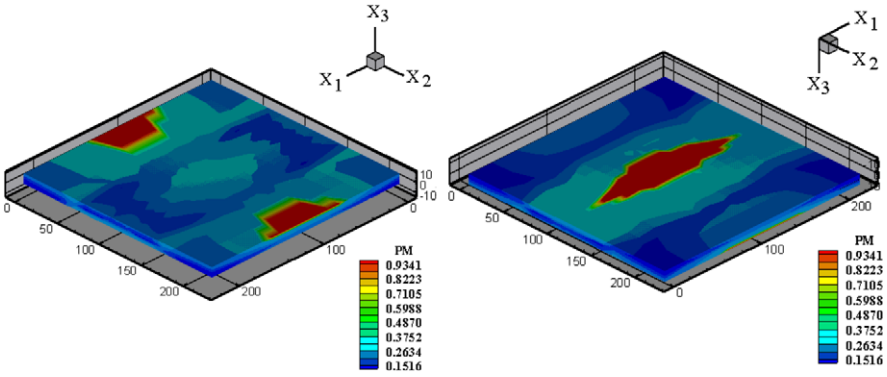

Fig. 17. Fringe plots of the matrix cracking damage variable in the specimen at $t = 160$ μs; left: top surface; right: bottom surface.

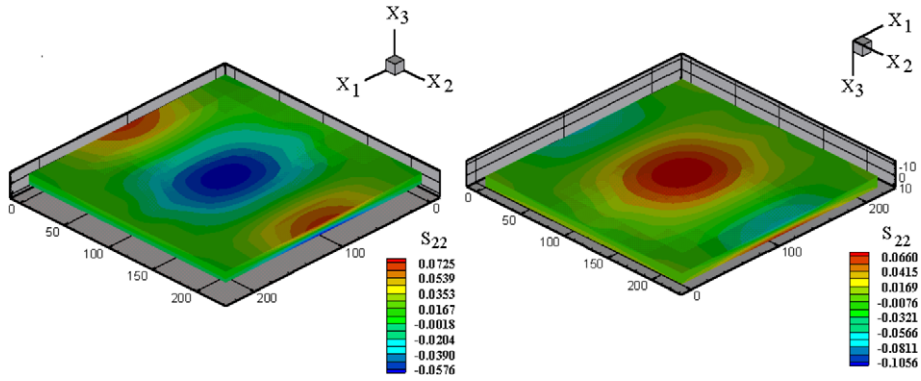

Fig. 18. Fringe plots of the normal stress (GPa), S_{22}, in the specimen at $t = 100$ μs; left: top surface; right: bottom surface.

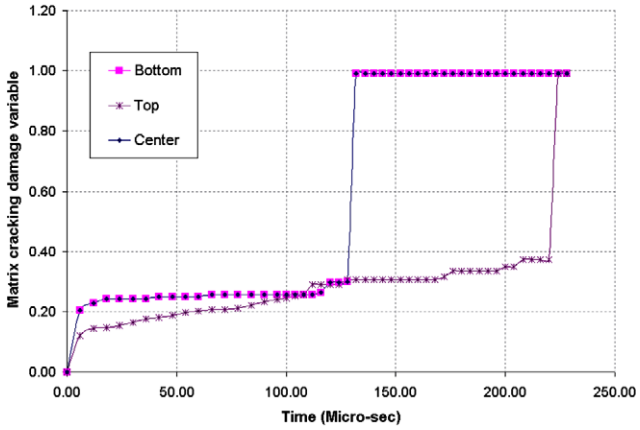

Fig. 19. Time histories of the matrix cracking damage variable at centroids of planes $X_3 = 0$ (bottom), $X_3 = 5$ mm (middle), and $X_3 = 10$ mm (top) with fibers oriented along the X_1-axis.

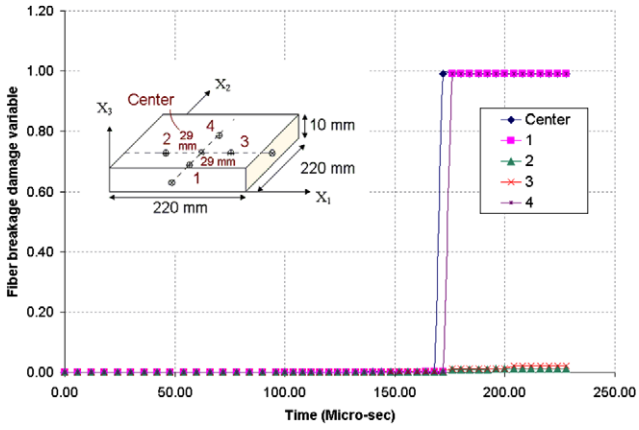

Fig. 21. Time histories, at five points on the middle surface, of evolution of the fiber breakage damage variable with fibers oriented along the X_1-axis.

fiber breakage is concentrated at points near the specimen's center that are along the X_2-axis. Furthermore, the fiber breakage variable, like the matrix cracking variable, also increases suddenly from essentially 0.0 to 1.0. Time histories of evolution of the fiber breakage damage variable at centroids of the top, the middle, and the bottom surfaces are given in Fig. 24; these suggest that the fiber breakage damage variable at the centroid of the top surface first develops gradually, and after it has reached the value 0.2 it grows very rapidly to 1.0. We emphasize that the quick growth of damage variables describing the fiber breakage and the matrix cracking depends upon the damage evolution Eqs. (7)–(9) and values of parameters determined from the experimental data. Other damage evolution equations will give results quantitatively different from but most likely qualitatively similar to those presented here. Fringe

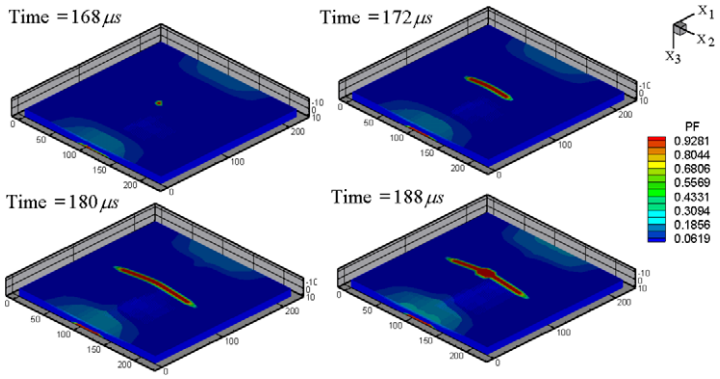

Fig. 20. Fringe plots of the fiber breakage damage variable, on the bottom surface, at four different times; PF stands for the fiber breakage damage variable.

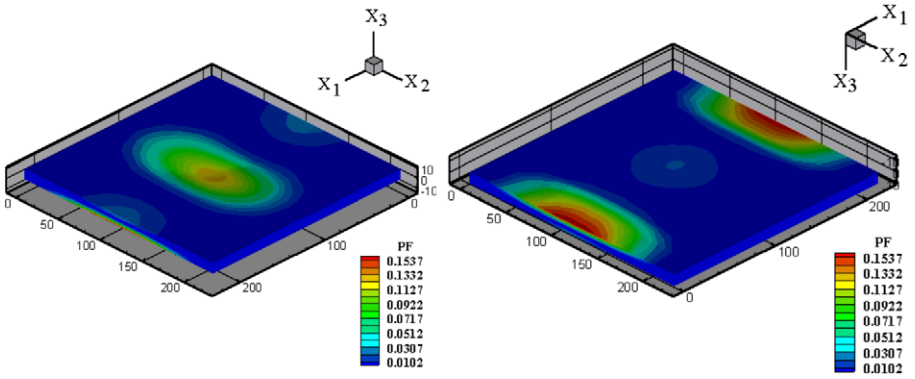

Fig. 22. Fringe plots of the fiber breakage damage variable at time = 160 μs; left: top surface; right: bottom surface.

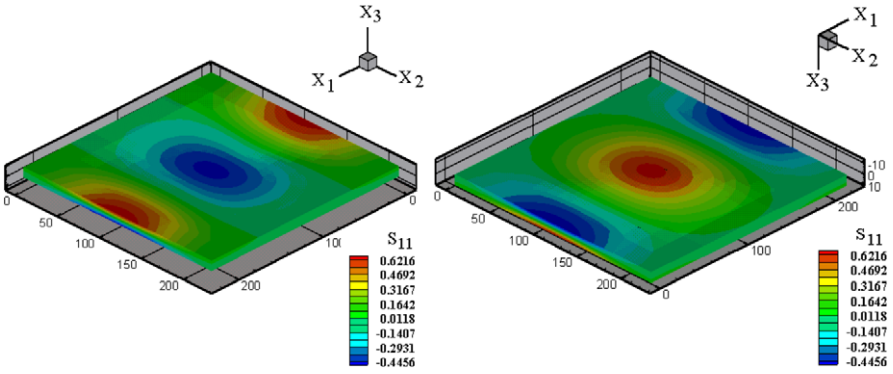

Fig. 23. Fringe plots of the longitudinal stress (GPa), S_{11}, at $t = 100$ μs; left: top surface; right: bottom surface.

plots, exhibited in Fig. 22, imply that the fiber breakage damage variable has high values at points of the top surface that are near the center, and at points near the edges that are also on the X_1-axis; however, the maximum value at any of these points at $t = 160$ μs is only about 0.15.

We conclude from fringe plots of the longitudinal (or the axial) stress, S_{11}, exhibited in Fig. 23, that equal and opposite values of S_{11} occur at corresponding points of the top and the bottom surfaces. The maximum magnitude of the longitudinal stress occurs at points near centroids of these surfaces, and also at points on the edge surfaces that are close to the X_1-axis. Whereas the axial stress is compressive at points near the centroid of the top surface, it is tensile at points close to the edge surfaces.

5.2.4. Delamination between adjoining layers

For the 0° plies and time $t = 220$ μs, Figs. 25–27 show, respectively, fringe plots of the fiber/matrix debonding, fiber breakage, and the matrix cracking damage variables on planes $X_1 = 110$ mm, and $X_2 = 110$ mm; delaminations between adjoining layers are depicted as solid lines. Since lines indicating the delamination do not pass continuously through the entire laminate, the delamination initiates from more than one point, not necessarily instantaneously, on an interface between two adjoining layers. At $t = 220$ μs, one or more of the three damage variables equal nearly 1 at every point of these two cross-sections.

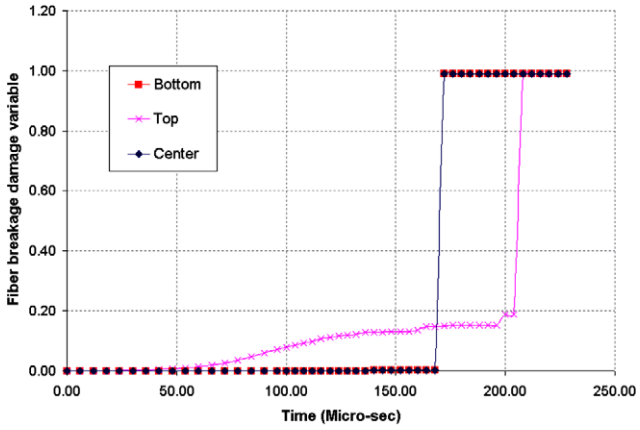

Fig. 24. Time histories of the fiber breakage damage variable at centroids of planes $X_3 = 0$ (bottom), $X_3 = 5$ mm (middle), and $X_3 = 10$ mm (top) with fibers oriented along the X_1-axis.

Fig. 28 shows the delaminated areas in all layers as seen from the top as if the composite were transparent. The area was approximated as rectangles, and its magnitude was calculated to be 6977 mm^2 and 4550 mm^2 for fiber orientations of 0° and 45° respectively. This method of calculating the delaminated area excludes overlapping delaminated areas, and underestimates the total delaminated area. Whereas one can ascertain in the numerical work delamination among adjoining layers, it is not clear how to do so experimentally.

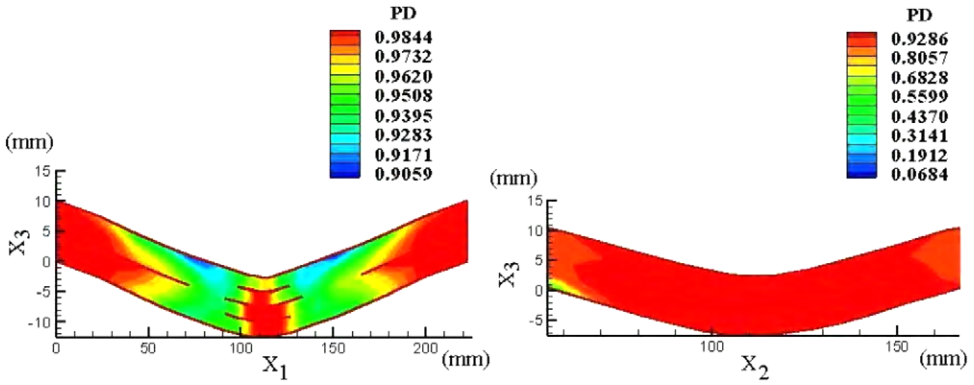

Fig. 25. Delamination/sliding between adjoining plies, and fringe plots of the fiber/matrix debonding damage variable on cross-sections $X_2 = 110$ mm (left figure), and $X_1 = 110$ mm (right figure) at $t = 220$ μs.

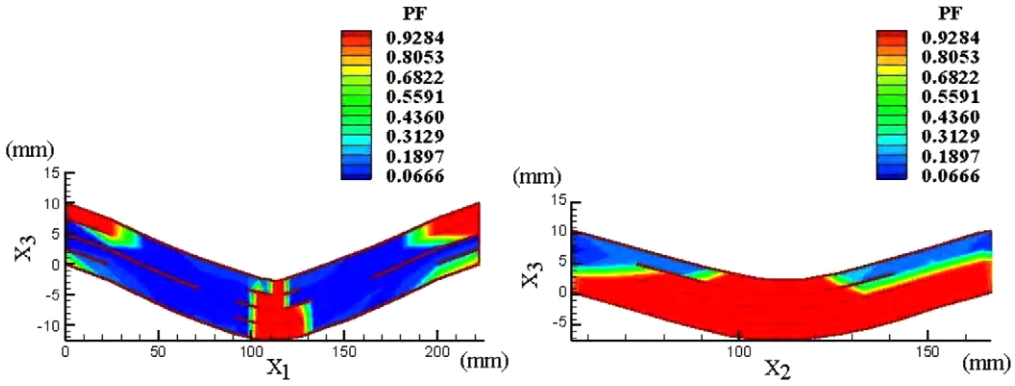

Fig. 26. Delamination/sliding between adjoining plies, and fringe plots of the fiber breakage damage variable on cross-sections $X_2 = 110$ mm (left figure), and $X_1 = 110$ mm (right figure) at $t = 220$ μs.

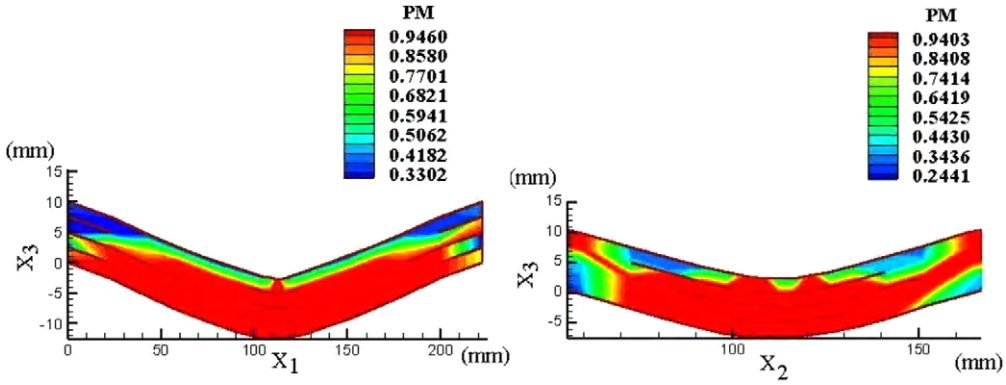

Fig. 27. Delamination/sliding between adjoining plies, and fringe plots of the matrix cracking damage variable on cross-sections $X_2 = 110$ mm (left figure), and $X_1 = 110$ mm (right figure) at $t = 220$ μs.

5.2.5. Energy dissipation

For each one of the four failure modes, Fig. 29 displays the total energy dissipated as a function of the fiber orientation angle. For all fiber orientation angles, the energy dissipated due to matrix cracking is miniscule as compared to that in any of the other three damage mechanisms; this is mainly due to low values of the elastic moduli of the matrix. With an increase in the fiber orientation angle from 0° to 45°, the energy dissipated due to delamination increases but those due to fiber/matrix debonding and matrix cracking decrease. An examination of the delamination initiation time revealed that it ensued earliest at 128 μs for fiber orientation of 0° or 90°, and latest at 140 μs for fiber orientation of 45°.

5.2.6. Effect of fiber orientation angle

Fig. 30 exhibits, for different fiber orientations, at time $t = 220$ μs, the total work done by external forces, the

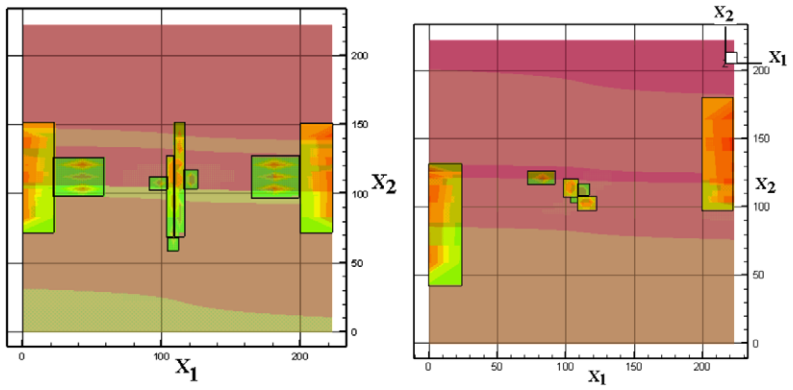

Fig. 28. Delaminated area as seen from the top surface of the composite; Left figure has fibers oriented at 0°, and the right figure has fibers oriented at 45°.

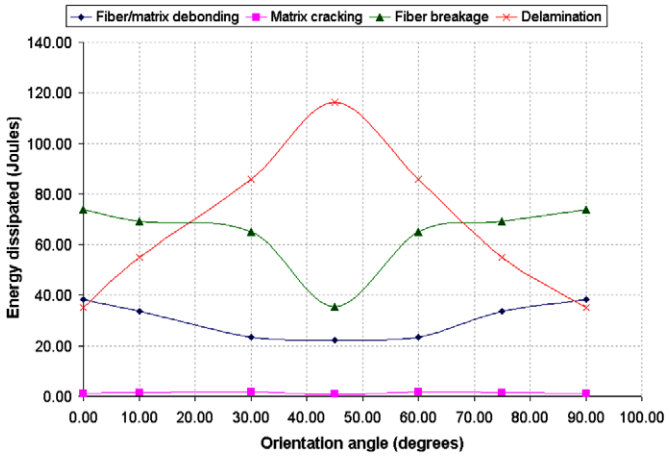

Fig. 29. Energy dissipated in different failure modes versus the fiber orientation angle.

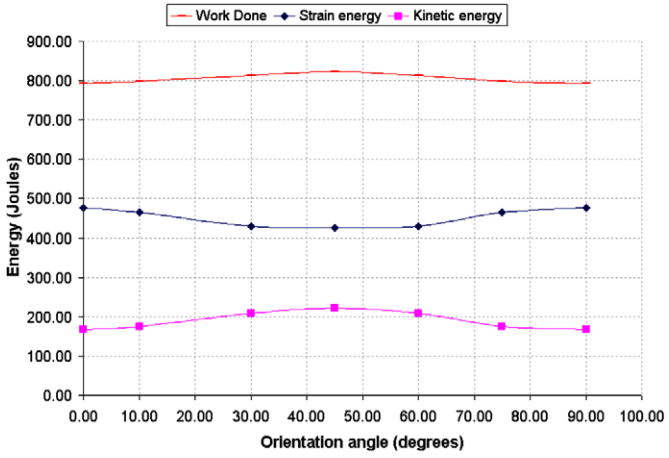

Fig. 30. Total work done, strain energy, and kinetic energy versus the fiber orientation angle.

strain energy of the deformed body, and the kinetic energy of the body calculated from Eqs. (23), (27) and (28) respectively. The balance of energy requires that the total work done by external forces equals the sum of the energy required to deform the body, strain energy of the body, kinetic energy of the body, and the energy dissipated in all failure mechanisms. For different fiber orientations, the percentage of work done by external forces dissipated in all failure modes is shown in the bar chart of Fig. 31; a high value of this ratio signifies that more of the total work done by external forces is dissipated in all of the failure modes, and the composite is more effective in resisting explosive loads. This ratio can be used to define the *Figure of Merit* of the composite. Thus clamped uni-directional AS4/PEEK composites with fiber orientations between 30° and 60° are equally effective in resisting explosive loads.

We note that the total work done (cf. Fig. 30) by external forces is virtually independent of the fiber orientation angle. With an increase in the fiber orientation angle from 0° to 45°, the energy required to deform the body decreases and the kinetic energy increases monotonically. The fraction of the total work done by external forces dissipated due to various failure mechanisms has the maximum value of nearly 22% for fiber orientations of 30° and 60°; thus plies with clamped edges and fiber orientations of 30° to 60° are good choices for optimizing the energy dissipation due to all failure modes. For these fiber orientations in the AS4/PEEK laminated composite clamped at all edges subjected to a pressure load on the top surface, the energy dis-

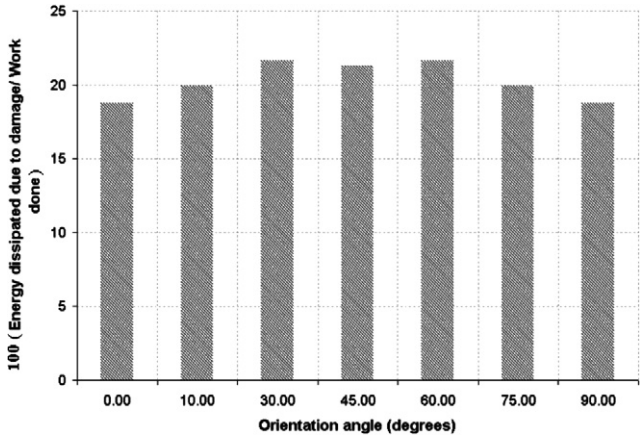

Fig. 31. For different fiber orientation angles, percentage of the work done by external forces dissipated in all failure modes.

sipated due to delamination exceeds that in each of the other three failure modes considered.

Another quantity of interest for dynamically loaded structural composites is the maximum lateral deflection. For seven fiber orientations considered in this work, Fig. 32 shows time histories of the vertical displacement of the specimen centroid. At $t = 220$ μs, the centroidal deflection is maximum for the 30° plies, and minimum for the 0° or the 90° laminates.

The preceding discussion of the damage evolution indicates that critical points to examine are centroids of the top and the bottom surfaces, and centers of the edges of the top and the bottom surfaces. In order to examine which failure mode initiates first in plies of different fiber orientations, we have plotted in Figs. 33–35 time histories of evolution, at specimen's centroid, of the three damage variables for different fiber orientation angles mentioned above. It is clear that the time of initiation of the fiber/matrix debonding is affected most by the fiber orientation, and that of fiber breakage least by the fiber orientation angle. The time of initiation and complete failure due to fiber breakage at

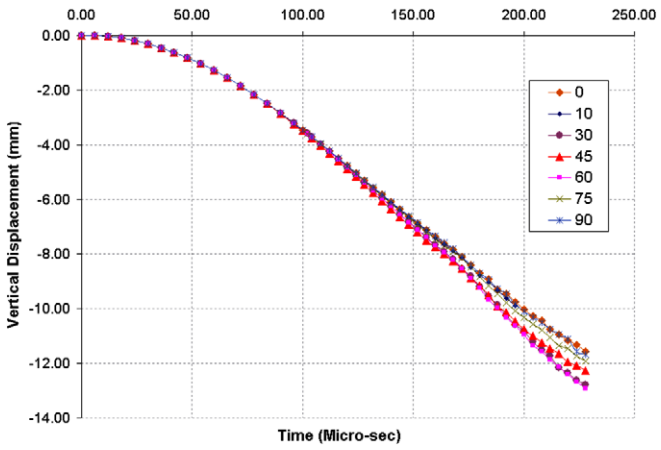

Fig. 32. For five fiber orientations, time histories of the deflection of the specimen centroid.

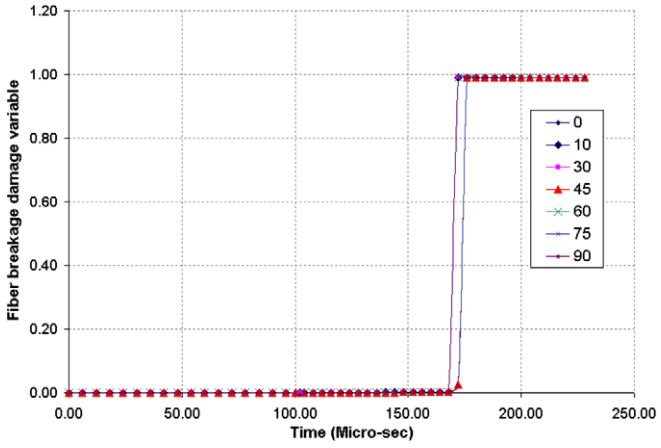

Fig. 33. Time histories of evolution of the fiber breakage damage variable at specimen's centroid for different fiber orientation angles.

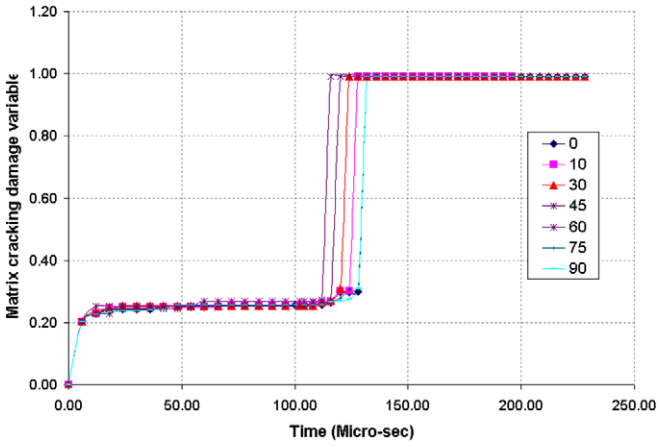

Fig. 34. Time histories of evolution of the matrix cracking damage variable at specimen's centroid for different fiber orientation angles.

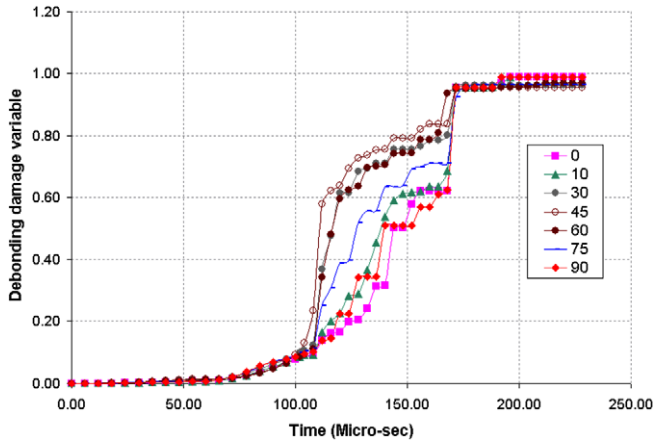

Fig. 35. Time histories of evolution of the fiber/matrix debonding damage variable at specimen's centroid for different fiber orientation angles.

specimen's centroid is virtually independent of the fiber orientation angle.

At time = 188 μs, Fig. 36 illustrates distributions of fiber breakage, matrix cracking and debonding variables in laminates with fiber orientation angles of 30°, 45° and 75°. The fiber breakage damage variable is spread perpendicular to the fibers, while the matrix cracking and debonding damage variables along the fibers. Thus the direction of propagation of the damage variables depends upon the fiber orientation angle.

5.2.7. Remarks

From a thorough examination of results computed for the present problem, one can draw the following conclusions regarding the order and the location of initiation of different failure modes in a clamped AS4/PEEK laminated composite subjected to blast loads on the top surface: (i) fiber/matrix debonding at edges of the bottom and the top surfaces that are perpendicular to fibers, (ii) matrix cracking at the centroid of the bottom surface, and at edges of the top surface that are perpendicular to fibers, (iii) fiber breakage at edges of the top surface that are parallel to

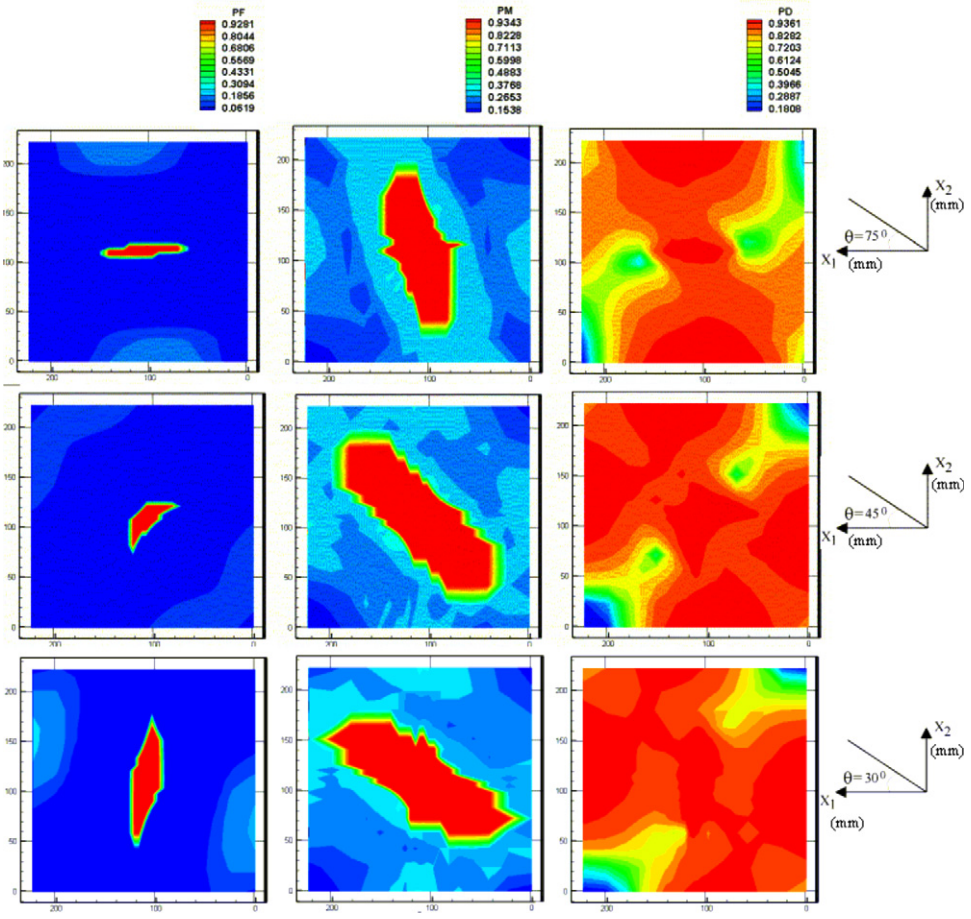

Fig. 36. At $t = 188$ μs, distribution of fiber breakage, matrix cracking and debonding variables in 30°, 45° and 75° laminates.

fibers, and then at the centroid of the bottom surface, (iv) debonding at centroids of the bottom and the top surfaces, (v) fiber breakage at the centroid of the top surface, (vi) fiber breakage at sides of the bottom surface, and (vii) matrix cracking at the centroid of the top surface. This information can be exploited in the design of laminates for attaining a designated functional objective. Results for other parameter variations are given in [42].

6. Limitations of the model

The three internal variables used here to model matrix cracking, fiber breakage, and fiber/matrix debonding do not account for fiber pull out, fiber kinking, fiber buckling,, and matrix crushing. Furthermore, they homogenize the effect of damage induced locally, enable one to compute energies dissipated in different failure modes, and allow for interaction among various failure modes. However, one can not compute the length of cracks, and lengths of fiber/matrix debonded zones.

In the analyses of various problems, the loading wave is taken to be plane which is the case for a large value of the stand-off distance. Also, the spatial variation of the pressure may not match well with what has been assumed here.

Values of material parameters given in Table 2 are for the AS4/PEEK composite, and all of the results have been computed for it. One should follow the procedure outlined in [23] to derive material parameters for other unidirectional fiber reinforced composites and then study their ballistic response. The mathematical model and results presented herein are not valid for woven and/or stitched composites, and for composites reinforced with randomly distributed short fibers.

7. Conclusions

We have developed a mathematical model for analyzing transient deformations of a composite subjected to shock loads produced by an underwater explosion, and a modular computer code, in Fortran, to find numerically an approximate solution of the pertinent initial-boundary-value problem. The problem formulation includes evolution of damage due to fiber breakage, fiber/matrix debonding, matrix cracking, and delamination. Energies dissipated in these failure modes are computed, and the effect on them of various parameters examined. The summary of results given below includes results presented in Ref. [42] but not included here.

It is found that approximately 20% of the total work done by external forces is dissipated in the four failure modes. Both for the clamped 0° and the 45° laminated composites, the energy dissipated due to delamination for clamped edges is nearly twice of that for simply supported edges. About 43% of the energy input into the structure is used to deform it, and the remaining 42% is converted into the kinetic energy. For simply supported laminates, these proportions strongly depend upon the fiber orientation angle.

The fiber orientation influences when and where each failure mode initiates and its direction of propagation. Debonding between fibers and the matrix occurs along the fibers rather than in a direction perpendicular to the fibers. For clamped edges, the debonding damage variable starts from the edges perpendicular to the fibers and propagates, along the fibers, towards the center; it propagates in the thickness direction instantaneously most likely due to thin laminates studied here in. Matrix cracking damage variable initiates first at the center of the back surface, where there are high tensile stresses developed, and propagates faster along the fibers than in the transverse direction. Fiber breakage is concentrated at points near the specimen's centroid that are along the X_2-axis. For all fiber orientations, the energy dissipated due to matrix cracking is miniscule as compared to that in any of the other three damage modes. The fraction of the total work done by external forces dissipated due to various failure mechanisms has the maximum value of nearly 22% for fiber orientations of 30° and 60°, of which ~10% is due to delamination. The stacking sequence also strongly influences energies dissipated in different failure modes.

The target thickness plays a role in determining which failure mode is dominant. The fraction of energy dissipated due to delamination failure mode decreases exponentially with an increase in the target thickness, and has the maximum value for the thinnest target.

Varying constituents' properties affects the initiation time of the damage modes. Increasing fiber's Young's modulus results in slightly different rates of evolution of the fiber/matrix debonding damage variable, and delays the initiation of the matrix cracking damage. Decreasing Young's modulus delays the initiation of the matrix cracking damage variable. Increasing fiber's shear modulus delays the initiation of the fiber breakage variable and enhances the initiation of the fiber/matrix debonding damage variable. Increasing the matrix shear modulus reduces noticeably specimen's centroidal deflection, enhances both the time of initiation and the rate of growth of the fiber/matrix debonding damage variable, and delays the initiation of the damage due to fiber breakage.

An increase in the fiber volume fraction decreases affinely the total work done by external forces, decreases parabolically the kinetic energy, and has virtually no effect on the energy required to deform the body.

For deformations caused by the explosion of a nuclear device, the composite fails very quickly due to complete delamination coupled with early initiation and rapid growth of the fiber/matrix debonding and matrix cracking, and very little centroidal deflection and fiber breakage.

Laminate's deformations for small values of the stand off distance are similar to those induced by a nuclear explosion.

Acknowledgements

This work was partially supported by the ONR grants N00014-98-1-3000 and N00014-06-1-0567 to Virginia Polytechnic Institute and State University (VPI& SU) with Dr. Y. D.S. Rajapakse as the program manager. Views expressed herein are those of authors, and neither of funding agencies nor of VPI& SU.

References

[1] Mouritz A. The effect of underwater explosion shock loading on the fatigue behaviour of GRP laminates. Composites 1995;26(1):3–9.
[2] Mouritz A. The damage to stitched GRP laminates by underwater explosion shock loading. Compos Sci Technol 1995;55(4):365–74.
[3] Mouritz A. The effect of underwater explosion shock loading on the flexural properties of GRP laminates. Int J Impact Eng 1996;18(2):129–39.
[4] Gellert E, Cimpoeru S, Woodward R. A study of the effect of target thickness on the ballistic perforation of glass-fibre-reinforced plastic composites. Int J Impact Eng 2000;24(5):445–56.
[5] Will MA, Franz T, Nurick GN. The effect of laminate stacking sequence of CFRP filament wound tubes subjected to projectile impact. Compos Struct 2002;58(2):259–70.
[6] Wen HM. Penetration and perforation of thick FRP laminates. Compos Sci Technol 2001;61:1163–72.
[7] Morais W, Monteiro S, d'Almeida J. Effect of the laminate thickness on the composite strength to repeated low energy impacts. Compos Struct 2005;70(2):223–8.
[8] Sierakowski R, Chaturvedi S. Dynamic loading and characterization of fiber reinforced composites. New York: John Wiley and Sons Inc; 1997.
[9] Espinosa H, Dwivedi S, Lu H. Modeling impact induced delamination of woven fiber reinforced composites with contact/cohesive laws. Comput Methods Appl Mech Eng 2000;183(3-4):259–90.
[10] Fu S, Mader E, Hu X, Yue C. Fracture resistance of short-glass-fiber-reinforced and short-carbon-fiber-reinforced polypropylene under charpy impact load and its dependence on processing. J Mater Process Technol 1999;89-90:501–7.
[11] Roy R, Sarkar BK, Bose NR. Impact fatigue of glass fibre–vinylester resin composites. Compos Part A: Appl Sci Manufactur 2000;32(6):871–6.
[12] Sjögren BA. Static strength of CFRP laminates with embedded fiber-optic edge connectors. Compos Part A: Appl Sci Manufactur 2001;32(2):189–96.
[13] Hull D, Shi Y. Damage mechanism characterization in composite damage tolerance investigations. Compos Struct 1993;23(2):99–120.
[14] Hitchen S, Kemp R. The effect of stacking sequence on impact damage in a carbon fibre/epoxy composite. Composites 1995;26(3):207–14.
[15] Habib F. A new method for evaluating the residual compression strength of composites after impact. Compos Struct 2001;53(3):309–16.
[16] Iannucci L, Dechaene R, Willows M, Degrieck J. A failure model for the analysis of thin woven glass composite structures under impact loadings. Comput Struct 2001;79:785–99.

[17] Shikhmanter L, Cina B, Eldror I. Fractography of CFRP composites damaged by impact and subsequently loaded statically to failure. Composites 1995;26(2):154–60.
[18] Parga-Landa B, Vlegels S, Hernández-Olivares F, Clark SD. An analytical study of the effect of slamming pressures on the interlaminar behaviour of composite panels. Compos Struct 1999;46(4) : 357–65.
[19] Dandekar DP, Beaulieu PA. Compressive and tensile strengths of glass reinforced polyester under shock wave propagation. In: High strain rate effects on polymers metal and ceramic matrix composites and other advanced materials. New York: ASME Press; 1995. p. 63–70.
[20] Schonberg W. Protecting spacecraft against orbital debris impact damage using composite materials. Compos Part A: Appl Sci Manufactur 2000;31(8):869–78.
[21] Mouritz A. Ballistic impact and explosive blast resistance of stitched composites. Compos Part B: Eng 2001;32(2):431–9.
[22] Nurick GN, Shave GC. The deformation and tearing of thin square plates subjected to impulsive loads—an experimental study. Int J Impact Eng 1996;18(1):99–116.
[23] Hassan NM, Batra RC. Modeling damage development in polymeric composites, Composites B, in press.
[24] Christensen R. Mechanics of composite materials: recent advances. - New York: Pergamon Press; 1982.
[25] Daniel I, Ishai O. Engineering mechanics of composite materials. New York: Oxford University Press; 1994.
[26] Herakovich C. Mechanics of fibrous composites. New York: John Wiley & Sons Inc; 1998.
[27] Jones R. Mechanics of composite materials. USA: Taylor & Francis Inc; 1999.
[28] Agarwal B, Broutman L. Analysis and performance of fiber composites. New York: Wiley; 1990.
[29] Batra RC. Elements of continuum mechanics. Reston, VA: AIAA; 2005.
[30] Batra RC. Comparison of results from four linear constitutive relations in isotropic finite elasticity. Int J Nonlinear Mech 2001;36:421–32.
[31] Kyriakides S, Arseculeratne R, Perry E, Liechti K. On the compressive failure of fiber reinforced composites. Int J Solids Struct 1995;32(6–7):689–738.
[32] Vogler T, Kyriakides S. Inelastic behavior of an AS4/PEEK composite under combined transverse compression and shear. Part I: Experiments. Int J Plasticity 1999;15(8):783–806.
[33] Hughes TJR. The finite element method. NJ: Prentice Hall; 1988.
[34] Türkmen HS, Mecitolu Z. Dynamic response of a stiffened laminated composite plate subjected to blast load. J Sound Vibr 1999;221(3):371–89.
[35] Comtois J, Edwards M, Oakes M. The effect of explosives on polymer matrix composite laminates. Compos Part A: Appl Sci Manufactur 1999;30(3):181–90.
[36] Langdon G, Cantwell W, Nurick G. The blast response of novel thermoplastic-based fibre-metal laminates – some preliminary results and observations. Compos Sci Technol 2005;65(6):861–72.
[37] Cole RH. Underwater explosions. Princeton: Princeton University Press; 1948.
[38] Liang C, Tai Y. Shock responses of a surface ship subjected to noncontact underwater explosions. Ocean Eng 2005:1–25.
[39] Bishop JH. Underwater shock standards and tests for naval vessels. DSTO Materials Research Laboratory, 1993.
[40] O'Hara GJ, Cunniff PF. Scaling for shock response of equipment in different submarines. Shock Vibr 1993;1(2):161–70.
[41] Luo R, Green E, Morrison C. An approach to evaluate the impact damage initiation and propagation in composite plates. Compos Part B: Eng 2001;32:513–20.
[42] Hassan, NM. Damage development in static and dynamic deformations of fiber-reinforced composite plates. PhD dissertation, Virginia Tech, 2006.